

Cosmology-dependent covariance in galaxy cluster number counts: consequences for parameter inference

Henrique C. N. Lettieri,¹ Mariana Penna-Lima,^{2,3,2} Sandro D. P. Vitenti^{1,3}

¹Departamento de Física, Universidade Estadual de Londrina, Rod. Celso Garcia Cid, Km 380, 86057-970, Londrina, Brasil

²Instituto de Física e Centro Internacional de Física, Universidade de Brasília, 70297-400, Brasilia, Brazil

³Programa de Pós-Graduação em Física, Universidade Estadual de Londrina, Rod. Celso Garcia Cid, Km 380, 86057-970, Londrina, Brazi

E-mail: henrique.cnl23@uel.br, pennalima@unb.br, vitenti@uel.br

Abstract. Galaxy clusters provide powerful constraints on cosmology through their abundance as a function of mass and redshift. Parameter inference from cluster counts requires modelling the data covariance entering the likelihood, including contributions from Poisson shot noise and super-sample covariance (SSC) induced by long-wavelength density fluctuations. While both the mean counts and their covariance depend on cosmology, evaluating the full covariance during parameter inference can be computationally expensive, particularly for SSC terms. As a result, many analyses adopt approximations in which the covariance is computed at a single fiducial cosmology, either from simulations or theoretical predictions, and kept fixed during inference. In this work, we investigate the impact of constructing the covariance matrix at an incorrect fiducial cosmology and quantify how this assumption propagates into the estimation of Ω_c , σ_8 , and w . We perform a systematic analysis in which the covariance is either varied consistently with the sampled cosmology or fixed at displaced cosmological models, and we also explore intermediate strategies in which selected components, such as the computationally expensive SSC term, are kept fixed while others vary. Our analysis includes observational effects relevant for optical surveys, including mass-proxy scatter and photometric redshift uncertainties, and focuses on configurations representative of LSST-like surveys. We find that the estimators of Ω_c , σ_8 , and w remain unbiased even when the covariance is constructed at an incorrect cosmology; however, fixing the covariance can lead to significant over- or underestimation of confidence regions. The magnitude and sign of this effect are primarily driven by amplitude-related parameters such as $\ln(10^{10}A_s)$ and S_8 , and for LSST-like surveys an inconsistent covariance specification can artificially modify the apparent S_8 tension inferred from cluster counts. We further show that a single covariance update evaluated at the recovered best-fit cosmology is sufficient to restore the correct uncertainties. These results indicate that while fixed-covariance approximations may remain adequate for some single-probe analyses, a fully cosmology-dependent treatment is required for consistent multi-probe studies.

Contents

1	Introduction	1
2	Cluster Counts	3
2.1	Theoretical predictions	3
2.1.1	Halo bias and its role in SSC	6
2.2	Likelihood	6
2.3	Covariance Matrix	7
3	Fiducial Models and Mock Cluster Catalogs	9
4	Analyses and Results	10
4.1	Covariance choices on a fixed mock	11
4.2	Combined parameter shifts	15
4.3	Forward and mirror configurations agree	16
4.4	Bias of the parameter estimators	18
4.5	Observational realism: mass proxy and photometric redshifts	19
4.6	S_8 tension	21
4.7	Covariance matrix fixed to the best-fit	26
5	Conclusions	27
A	Estimation of Posterior Credible Volumes from MCMC Chains	30

1 Introduction

Galaxy cluster number counts are a powerful probe of cosmology, as the abundance of massive halos and their spatial distribution are sensitive to both the growth of structure and the expansion history of the Universe [1, 2]. A key challenge, however, is that cluster mass is not directly observable. Cluster samples are therefore selected through mass proxies such as X-ray observables, optical richness, gravitational lensing, and Sunyaev-Zel’dovich (SZ) signals, whose connection to the underlying halo mass must be modelled statistically through a mass-observable relation. In millimetre and X-ray surveys, where cluster catalogs typically contain at most a few hundred to a few thousand objects, cosmological analyses are often performed using Poisson-based likelihoods [3, 4], sometimes in an effectively unbinned form [5–9].

Wide-field optical surveys, on the other hand, have entered a regime of much larger cluster samples. Surveys such as the Sloan Digital Sky Survey (SDSS) [10, 11], the Dark Energy Survey (DES) [12, 13], Javalambre Physics Accelerating Universe Astrophysical Survey (J-PAS) [14, 15], and the Stage IV Vera C. Rubin Observatory Legacy Survey of Space and Time (LSST) [16] and *Euclid* [17] detect tens of thousands of clusters selected primarily through optical richness, also focusing on mass calibration provided by weak gravitational lensing measurements. In this high-count regime, analyses are commonly performed assuming a Gaussian likelihood in bins of observed richness and photometric redshift, both for computational convenience and to enable a consistent treatment of correlated uncertainties. Similar considerations apply to next-generation X-ray surveys such as SRG/eROSITA, which will deliver cluster catalogs of comparable statistical power [18].

Independently of whether one adopts a binned or an unbinned likelihood, the practical implementation of cluster number count analyses remains computationally demanding. The theoretical predictions

require evaluating multi-dimensional integrals over the true halo mass and redshift, as well as over observational quantities such as photometric redshift estimates and mass proxies, each described by their own probability distributions [5, 6, 11]. In addition to modelling the mean counts, a consistent likelihood must include an accurate description of the covariance matrix.

The covariance of cluster counts is composed of a shot-noise (Poisson) contribution and a SSC term [19–25]. The SSC arises from long-wavelength density fluctuations larger than the survey footprint, which modulate the local growth of structure and induce correlations across mass and redshift bins. Its incorporation into cluster-count likelihoods has motivated significant theoretical developments, including the formalism of Refs. [20, 26] and extensions beyond purely Gaussian approximations [27, 28]. For Stage IV surveys such as LSST, *Euclid* and SRG/eROSITA [28–30], where statistical errors are substantially reduced, an accurate treatment of SSC and of the full covariance structure becomes essential.

Despite these advances, consistently incorporating cosmology-dependent covariance terms remains challenging. The mean cluster counts depend on cosmology through the halo mass function and comoving volume element, while the SSC term further depends on halo bias and the large-scale matter power spectrum amplitude. As a result, both the mean signal and its covariance are intrinsically cosmology-dependent. In unbinned likelihoods, correlations across mass and redshift must be handled in a computationally efficient manner, while in binned Gaussian approaches the covariance matrix must be evaluated and inverted repeatedly during parameter inference. These challenges have motivated approximate treatments and fast covariance estimators [24, 26, 28, 31], as well as alternative statistical frameworks such as simulation-based or likelihood-free inference approaches [32–36].

In practice, computational efficiency is essential in multi-probe large-scale-structure analyses. To fully exploit the available data and mitigate systematic uncertainties, one of the primary goals of surveys such as the DES, LSST, and *Euclid* is to combine galaxy clustering, weak lensing, cluster clustering, number counts, and their cross-correlations within a unified framework [12, 13, 37, 38].

The computation of the covariance matrix relies either on data-driven approaches or on numerical simulations [39–44], which are generally generated at a single fiducial cosmology, or on (semi-)analytical calculations [20, 21]. The validity of this approximation must be reassessed as surveys enter a precision regime in which systematic effects and modelling assumptions contribute at a level comparable to (or even exceeding) the statistical uncertainties [40, 41, 44, 45].

Several studies have emphasized that super-sample covariance can significantly affect parameter uncertainties [22, 26]. In the context of weak lensing and large-scale structure, the cosmology dependence of the covariance has been shown to modify confidence regions at a non-negligible level [41, 44, 45].

However, the impact of cosmology-dependent covariance modelling on cluster number count analyses has not yet been systematically quantified in realistic observational scenarios.

In the cluster context, Fumagalli et al. [29] compared constraints on the matter density parameter Ω_m and on the amplitude of matter density fluctuations σ_8 obtained using a covariance matrix derived from simulations and an analytical one. Since both covariance matrices were fixed to a fiducial cosmology, they further explored the impact of adopting two additional (incorrect) cosmologies in place of the fiducial model. They showed that using an inconsistent covariance matrix can lead to either an underestimation or an overestimation of parameter uncertainties. However, their analysis was restricted to idealized halo catalogs with true masses and redshifts. Moreover, because the cosmological inference was performed on a single realization, it is not possible to evaluate the bias of the estimators in a statistical sense (see, e.g., [46]).

The impact of covariance modelling is particularly relevant in light of the so-called σ_8 or S_8 tension [47, 48], which refers to the discrepancy between the amplitude of matter fluctuations inferred from early-Universe probes, such as the cosmic microwave background, and that obtained from late-time large-scale-structure measurements [13, 49–52]. The parameter $S_8 \equiv \sigma_8 \sqrt{\Omega_m/0.3}$ is often used to characterize this tension, as it approximately follows the degeneracy direction of low-redshift probes. Since cluster abundance measurements are highly sensitive to both σ_8 and Ω_m , inaccuracies in the covariance

modelling can artificially broaden or shrink confidence regions in the σ_8 - Ω_m plane, potentially affecting the interpretation of consistency (or tension) between different cosmological datasets (see, e.g., [53] and references therein).

Motivated by these considerations, we adopt a forward-modelling approach to systematically assess the impact of a cosmology-dependent covariance matrix on cluster cosmological constraints. Using the NumCosmo [54] framework, whose C-based implementation enables the repeated evaluation of the cluster pipeline and covariance modelling required for this study, we generate mock cluster catalogs and compare analyses performed with fixed and varying covariance matrices. This allows us to quantify potential biases in the estimators of the cold dark matter density parameter Ω_c , σ_8 , and the dark energy equation-of-state parameter w , as well as changes in their inferred uncertainties.

Our analysis is carried out in different observational scenarios, including idealized catalogs with true masses and redshifts, as well as more realistic cases incorporating mass-observable relations and photometric redshift uncertainties. This allows us to evaluate the robustness of our conclusions under progressively more realistic assumptions.

We further investigate how fixing the covariance matrix to an incorrect cosmology influences the derived σ_8 and S_8 constraints and their interpretation in the context of current tension discussions. Finally, we analyze the effect of recomputing the covariance matrix at the best-fit parameters obtained from an initial analysis with an incorrect covariance model.

This paper is organized as follows. In section 2, we introduce the theoretical framework for cluster number counts, including the associated likelihood and covariance matrix, and describe their dependence on the underlying cosmological model. In section 3, we present the construction of the mock catalogs and the different observational scenarios considered in this analysis. The results are discussed in section 4, and we summarize our conclusions in section 5.

2 Cluster Counts

In this section, we present the theoretical framework for modelling cluster number counts, i.e. the one-point statistics of the cluster distribution, over a survey region of solid angle Ω_{sky} , and describe its dependence on the underlying cosmological parameters. We then account for the impact of SSC, which arises from density fluctuations on scales larger than the survey volume and induces additional correlations in the number counts. In the following subsections, we define the Gaussian likelihood adopted in this work to connect the theoretical predictions to the mock cluster catalogs, and describe how SSC is incorporated into the covariance of this likelihood.

2.1 Theoretical predictions

The theoretical modelling of cluster number counts is based on the halo mass function, which describes the comoving number density of dark matter halos per logarithmic mass interval at a given redshift. It is defined as

$$\frac{dn(M, z)}{d \ln M} = \frac{\bar{\rho}_m}{M} \nu f(\nu) \frac{d \ln \nu}{d \ln M}, \quad (2.1)$$

where $\bar{\rho}_m$ is the mean comoving matter density of the Universe and $f(\nu)$ is the multiplicity function. In this work, we adopt the multiplicity function calibrated by Tinker et al. [55], which provides an accurate description of halo abundances over a wide range of masses and redshifts.¹ The peak height is defined as $\nu \equiv \delta_c / \sigma_R(z)$ with δ_c denoting the critical linear overdensity for collapse and $\sigma_R^2(z)$ the variance of the linear matter density field smoothed with a top-hat filter of radius R associated with the halo mass.

The value of δ_c depends on the assumed collapse dynamics and may, in general, show a mild dependence on redshift and cosmology. An accurate interpolation capturing this behaviour is provided in

¹Alternative prescriptions, such as that of Despali et al. [56], may become relevant for future wide-area surveys.

[57]. In this work, we adopt the spherical top-hat collapse model, for which δ_c is approximately universal, and we fix its value to $\delta_c = 1.686$.

The variance of the smoothed linear density field is computed as

$$\sigma_R^2(z) = \int_0^\infty \frac{dk}{2\pi^2} k^2 P(k, z) |W(k, R)|^2, \quad (2.2)$$

where $P(k, z)$ is the linear matter power spectrum extrapolated to redshift z , and $W(k, R)$ is the Fourier transform of the window function. Throughout this analysis, we employ a real-space top-hat filter, whose Fourier-space representation is

$$W(k, R) = \frac{3}{kR} j_1(kR), \quad (2.3)$$

with j_1 denoting the spherical Bessel function of first order.

The smoothing scale R is related to the halo mass through a spherical overdensity definition,

$$M_\Delta = \frac{4\pi}{3} R_\Delta^3 \Delta \rho_c, \quad (2.4)$$

where ρ_c is the critical density of the Universe. In this work, cluster masses are defined with respect to an overdensity threshold of $\Delta = 200$.

The linear matter power spectrum is modelled as

$$P(k, z) = A_s k^{n_s} T^2(k) D^2(z), \quad (2.5)$$

where A_s is the amplitude of the primordial power spectrum, n_s is the scalar spectral index, $T(k)$ is the matter transfer function, and $D(z)$ is the linear growth factor normalized to unity at the present epoch [46]. Throughout this work, we adopt the Eisenstein-Hu transfer function [58]. This approximation provides a fast evaluation of the linear matter power spectrum and is sufficient for the purposes of this work, since both the mock catalogs and the parameter inference are performed consistently using the same modelling. In analyses of real observational data, a more accurate calculation of the linear power spectrum (e.g. using Boltzmann solvers such as CLASS or CAMB) would be required.

While A_s directly controls the normalization of the primordial power spectrum, it is common in cluster abundance analyses to express this normalization in terms of the root-mean-square fluctuation of the matter density field smoothed on a scale of $8 h^{-1} \text{Mpc}$, denoted by σ_8 . The two quantities are related by

$$A_s = \frac{\sigma_8^2}{\int_0^\infty \frac{dk}{2\pi^2} k^{n_s+2} T^2(k) W^2(k, 8 h^{-1} \text{Mpc})}. \quad (2.6)$$

With the ingredients introduced above, the halo mass function in eq. (2.1) provides the theoretical prediction for the abundance of galaxy clusters as a function of true mass and redshift. In practice, however, cluster masses are not directly observable. Cluster surveys infer masses through one or more observables (mass proxies), whose relation to the true halo mass is described statistically by the conditional distribution $P(M_{\text{obs}} | M, z)$.

Similarly, cluster redshifts can be measured either spectroscopically or photometrically. While spectroscopic redshifts are highly precise, photometric redshifts allow much larger samples at the cost of an additional scatter with respect to the true redshift. This uncertainty is modelled through the photo- z distribution $P(z_{\text{ph}} | z)$.

Taking these observational effects into account, the predicted distribution of clusters in observed mass and redshift is obtained by convolving the halo mass function with the mass-observable and photometric redshift relations:

$$x(M_{\text{obs}}, z_{\text{ph}}) = \Omega_{\text{sky}} \int d \ln M \int dz \frac{d^2 V}{dz d\Omega} \frac{dn(M, z)}{d \ln M} P(M_{\text{obs}} | M, z) P(z_{\text{ph}} | z), \quad (2.7)$$

where $d^2V/(dz d\Omega)$ is the comoving volume element per unit solid angle.

Binned cluster number counts

Rather than analysing the full continuous (unbinned) distribution, we perform a binned analysis in observed mass and photometric redshift. The expected number of clusters in a bin $[M_{\text{obs},i}, M_{\text{obs},i+1}]$ and $[z_{\text{ph},\alpha}, z_{\text{ph},\alpha+1}]$ is given by

$$\bar{\mu}_{i,\alpha} = \int_{M_{\text{obs},i}}^{M_{\text{obs},i+1}} \int_{z_{\text{ph},\alpha}}^{z_{\text{ph},\alpha+1}} x(M_{\text{obs}}, z_{\text{ph}}) dM_{\text{obs}} dz_{\text{ph}}. \quad (2.8)$$

In order to isolate the impact of SSC, we consider three levels of realism in the construction of mock catalogs. First, we analyze the idealized case of true masses and redshifts, corresponding to delta-function relations

$$P(M_{\text{obs}} | M, z) = \delta(M_{\text{obs}} - M), \quad P(z_{\text{ph}} | z) = \delta(z_{\text{ph}} - z). \quad (2.9)$$

We then progressively include mass-proxy scatter and photometric redshift uncertainties.

Mass-observable relation

To model the mass-proxy uncertainty, we adopt a log-normal relation between the true halo mass and the cluster richness λ , described by

$$P(\ln \lambda | M, z) = \frac{1}{\sqrt{2\pi} \sigma(M, z)} \exp\left[-\frac{(\ln \lambda - \mu(M, z))^2}{2\sigma^2(M, z)}\right], \quad (2.10)$$

$$\mu(M, z) = \mu_0 + \mu_M \ln\left(\frac{M}{M_0}\right) + \mu_z \ln\left(\frac{1+z}{1+z_0}\right), \quad (2.11)$$

$$\sigma(M, z) = \sigma_0 + \sigma_M \ln\left(\frac{M}{M_0}\right) + \sigma_z \ln\left(\frac{1+z}{1+z_0}\right). \quad (2.12)$$

In a full self-calibration approach, these nuisance parameters would be jointly constrained with cosmology. In this work, however, we keep them fixed in order to focus on the impact of SSC.

Photometric redshift uncertainties

Photometric redshift measurements introduce an additional source of uncertainty in the observed cluster distribution, as the inferred redshift z_{ph} differs from the true redshift z due to measurement scatter. We model this effect through a conditional probability distribution $P(z_{\text{ph}} | z)$, assumed to be Gaussian with zero mean bias,

$$P(z_{\text{ph}} | z) = \frac{1}{\sqrt{2\pi} \sigma^{\text{ph}}(z)} \exp\left[-\frac{(z_{\text{ph}} - z)^2}{2\sigma^{\text{ph}}(z)^2}\right]. \quad (2.13)$$

The photometric redshift scatter is taken to increase with redshift according to

$$\sigma^{\text{ph}}(z) = \sigma_0^{\text{ph}} (1+z), \quad (2.14)$$

where σ_0^{ph} sets the overall normalization of the photo- z uncertainty. In this work, we assume an unbiased photometric redshift relation and keep σ_0^{ph} fixed in all analyses.

Including this photo- z probability distribution in eq. (2.7) accounts for the migration of clusters across redshift bins induced by photometric measurement scatter.

2.1.1 Halo bias and its role in SSC

Galaxy clusters are biased tracers of the underlying matter density field [59]. In particular, the abundance of halos within a finite survey volume is sensitive to long-wavelength density fluctuations: a region that is slightly overdense with respect to the cosmic mean effectively lowers the threshold for collapse and enhances the formation of massive objects, leading to an excess of clusters relative to the global expectation from the halo mass function alone. This modulation is quantified by the halo bias function $b(M, z)$, which describes how halos of mass M trace large-scale matter perturbations.

Since the halo bias can be constructed consistently within the same framework used to model the halo mass function (e.g. [60]), we adopt the fitting function calibrated in [61], matching our choice of multiplicity function. The halo bias plays a central role in the SSC contribution to the cluster counts covariance, as it governs the response of the number counts to background density modes larger than the survey window.

In direct analogy with the predicted binned abundance $\bar{\mu}_{i,\alpha}$, we define the effective halo bias in each observed mass and photometric redshift bin (i, α) as the abundance-weighted average of $b(M, z)$,

$$b_{i,\alpha} = \frac{\Omega_{\text{sky}}}{\bar{\mu}_{i,\alpha}} \int_{M_{\text{obs},i}}^{M_{\text{obs},i+1}} \int_{z_{\text{ph},\alpha}}^{z_{\text{ph},\alpha+1}} dM_{\text{obs}} dz_{\text{ph}} \int d \ln M \int dz \frac{d^2 V}{dz d\Omega} \frac{dn(M, z)}{d \ln M} \times P(M_{\text{obs}}|M, z) P(z_{\text{ph}}|z) b(M, z). \quad (2.15)$$

In practice, evaluating this quantity requires the same multidimensional convolutions over mass and redshift that appear in the predicted cluster abundance $\bar{\mu}_{i,\alpha}$. Because these integrals must be computed for each bin and for every sampled cosmology, the effective bias constitutes one of the dominant computational costs of the pipeline. It enters explicitly in the SSC contribution to the covariance matrix, where super-survey density fluctuations couple coherently to the cluster number counts through $b_{i,\alpha}$, inducing correlations across mass and redshift bins.

2.2 Likelihood

The next step is to connect the theoretical predictions for the binned cluster number counts, $\bar{\mu}_{i,\alpha}$, to the observed data (or mock catalogues) in order to constrain the cosmological parameters.

The expression for the likelihood requires specifying the statistical model that links the discrete observed counts to the underlying matter distribution. In the standard approach, one assumes that the cluster counts arise from a Poisson sampling of a continuous underlying density (or intensity) field. Given this field, the expected number of objects in each bin, $\bar{\mu}_{i,\alpha}$, is fixed, and the counts in different bins are statistically independent. In this sense, the Poisson model assumes that all correlations between bins are fully encoded in the deterministic prediction for $\bar{\mu}_{i,\alpha}$.

Under these assumptions, the probability of observing a discrete number of clusters in each bin is described by a Poisson likelihood,

$$\mathcal{L}_{\text{P}}(N|\bar{\mu}) = \prod_{i=1}^{B_M} \prod_{\alpha=1}^{B_z} \frac{\bar{\mu}_{i,\alpha}^{N_{i,\alpha}} e^{-\bar{\mu}_{i,\alpha}}}{N_{i,\alpha}!}, \quad (2.16)$$

where B_M and B_z denote the number of mass and redshift bins, respectively, $N_{i,\alpha}$ is the observed number of clusters in bin (i, α) , and $\bar{\mu}_{i,\alpha}$ is the theoretical prediction given by eq. (2.8).

This likelihood is conditional on the underlying density field, i.e., it assumes that the expected counts $\bar{\mu}_{i,\alpha}$ are fixed quantities. In that case, the counts in different bins are independent. In practice, however, the density field is itself described statistically, and therefore the expected counts $\bar{\mu}_{i,\alpha}$ inherit this stochasticity and should be treated as random variables with a joint distribution $P(\bar{\mu})$ induced by the

underlying field. The Poisson model then holds only conditionally, $P(N|\bar{\mu})$, and the full likelihood is obtained by marginalizing over $\bar{\mu}$,

$$P(N) = \int d\bar{\mu} P(\bar{\mu}) \prod_{i,\alpha} \frac{\bar{\mu}_{i,\alpha}^{N_{i,\alpha}} e^{-\bar{\mu}_{i,\alpha}}}{N_{i,\alpha}!}. \quad (2.17)$$

In this formulation, correlations between bins arise from the joint distribution $P(\bar{\mu})$, even though the counts are conditionally independent given $\bar{\mu}$. In general, this marginal likelihood does not admit a simple closed form, which makes an exact treatment of SSC challenging.

Approximate schemes have therefore been developed. In particular, [24] proposes a systematic expansion that captures the effect of these fluctuations on the likelihood. In the following, we adopt a similar approach.

In the regime where the expected counts per bin are sufficiently large, the marginal likelihood can be approximated by matching its first two moments (mean and covariance), leading to a multivariate Gaussian description. We therefore adopt the Gaussian likelihood

$$\mathcal{L}_G(N) = \frac{1}{\sqrt{(2\pi)^B \det C}} \exp\left[-\frac{1}{2} (N - \langle \bar{\mu} \rangle)^T C^{-1} (N - \langle \bar{\mu} \rangle)\right], \quad (2.18)$$

where $B = B_M \times B_z$ is the total number of bins, $\langle \bar{\mu} \rangle = \langle N \rangle$ is the mean number of clusters under $P(\bar{\mu})$, which follows directly from eq. (2.17), and C is the covariance matrix of the binned counts, including both Poisson and super-sample contributions. In this formulation, the impact of SSC is entirely captured through additional contributions to the covariance matrix, as discussed in the next subsection.

2.3 Covariance Matrix

In the Gaussian approximation adopted in this work, all the information about statistical fluctuations in the cluster number counts is encoded in the covariance matrix. From eq. (2.17), the covariance of the counts can be written exactly as ²

$$\text{Cov}(N_{i\alpha}, N_{j\beta}) = \delta_{ij} \delta_{\alpha\beta} \langle \bar{\mu}_{i\alpha} \rangle + \text{Cov}(\bar{\mu}_{i\alpha}, \bar{\mu}_{j\beta}), \quad (2.19)$$

where the first term corresponds to Poisson shot noise, and the second term arises from fluctuations of the underlying density field. This decomposition follows directly from the hierarchical model in eq. (2.17) and does not rely on any approximation.

The Gaussian approximation consists in assuming that the likelihood is fully characterized by the first two moments of the counts. Under this assumption, the expression above provides all the information required to construct the likelihood, and the problem reduces to computing the covariance of the expected counts, $\text{Cov}(\bar{\mu}_{i\alpha}, \bar{\mu}_{j\beta})$.

Accordingly, we write the covariance matrix as the sum of a shot-noise contribution and a term encoding correlations induced by the underlying density field,

$$C_{i\alpha, j\beta} = C_{i\alpha, j\beta}^{\text{SN}} + C_{i\alpha, j\beta}^{\text{field}}, \quad (2.20)$$

with

$$C_{i\alpha, j\beta}^{\text{SN}} = \delta_{ij} \delta_{\alpha\beta} \langle \bar{\mu}_{i\alpha} \rangle \quad (2.21)$$

and $C_{i\alpha, j\beta}^{\text{field}} = \text{Cov}(\bar{\mu}_{i\alpha}, \bar{\mu}_{j\beta})$.

In general, $C_{i\alpha, j\beta}^{\text{field}}$ receives contributions from a broad range of scales and depends on the survey geometry and binning scheme. A full evaluation requires integrating the two-point statistics of the density field over the survey window.

²For simplicity, hereafter we drop the comma between the mass and redshift indices, i.e., $\bar{\mu}_{i,\alpha} \equiv \bar{\mu}_{i\alpha}$.

In the following, we approximate this term by retaining only the contribution from long-wavelength modes of the density field, leading to the SSC approximation. These modes coherently modulate the expected counts across the survey volume, inducing correlations between different bins. Under this approximation, the field covariance is written as

$$C_{i\alpha,j\beta}^{\text{field}} \approx C_{i\alpha,j\beta}^{\text{SSC}} = b_{i\alpha} \langle \bar{\mu}_{i\alpha} \rangle b_{j\beta} \langle \bar{\mu}_{j\beta} \rangle S_{\alpha\beta}, \quad (2.22)$$

where $b_{i\alpha}$ is the effective halo bias averaged over bin (i, α) , and $S_{\alpha\beta}$ quantifies the covariance of the long-wavelength density fluctuations between redshift bins α and β , averaged over the survey volume.

More generally, the cross-correlation of the matter density contrast at two redshifts can be written as

$$\sigma^2(z_1, z_2) \equiv \langle \delta(z_1) \delta(z_2) \rangle = \int \frac{d^3k}{(2\pi)^3} P(k, z_1, z_2) W(\mathbf{k}, z_1) W^*(\mathbf{k}, z_2), \quad (2.23)$$

where $P(k, z_1, z_2)$ is the unequal-time matter power spectrum and $W(\mathbf{k}, z)$ is the Fourier transform of the survey window function.

In general, the window function encodes the survey geometry and selection, including the angular footprint, masking, and radial binning. Because W couples angular and radial modes, evaluating eq. (2.23) directly becomes computationally demanding and strongly survey dependent.

To address this, we follow the approach developed in [26], where the covariance is expanded in spherical harmonics. In this formalism, the clustering and geometrical contributions factorize, and the dependence on the matter power spectrum is captured by the angular matter power spectrum,

$$C_\ell^m(z_1, z_2) = \frac{2}{\pi} \int dk k^2 j_\ell(kr_1) j_\ell(kr_2) P(k, z_1, z_2), \quad (2.24)$$

where j_ℓ denotes the spherical Bessel function and r_i is the comoving distance corresponding to redshift z_i .

The survey geometry enters separately through an angular window power spectrum $C_\ell(W)$, such that the covariance can be written as

$$\sigma^2(z_1, z_2) = \frac{1}{\Omega_{\text{sky}}^2} \sum_\ell (2\ell + 1) C_\ell(W) C_\ell^m(z_1, z_2). \quad (2.25)$$

This expression corresponds to the general partial-sky case, where masking and survey boundaries induce mode coupling through $C_\ell(W)$.

In this work, since our goal is not to model the impact of complex survey masks, we adopt the full-sky approximation. In this limit, the window function is constant on the sky, and its angular power spectrum is non-zero only for the monopole, $C_\ell(W) \propto \delta_{\ell 0}$. As a result, the sum over multipoles reduces exactly to the $\ell = 0$ term, yielding

$$\sigma_{\text{fullsky}}^2(z_1, z_2) = \frac{2}{\pi \Omega_{\text{sky}}^2} \int dk k^2 j_0(kr_1) j_0(kr_2) P(k, z_1, z_2). \quad (2.26)$$

This expression follows directly from the general formulation and does not involve any approximation beyond the assumption of full-sky coverage. It provides the exact covariance of the density contrast projected over the survey volume.

Finally, the matrix $S_{\alpha\beta}$ entering eq. (2.22) is obtained by averaging this expression over the redshift bins of the likelihood,

$$S_{\alpha\beta} = \int \frac{dV_1}{V_\alpha} \int \frac{dV_2}{V_\beta} \sigma_{\text{fullsky}}^2(z_1, z_2), \quad (2.27)$$

where V_α denotes the comoving volume of redshift bin α . In this step, we isolate the contribution of modes that are coherent over the survey volume, effectively averaging over smaller-scale fluctuations and retaining only the large-scale component that enters the SSC approximation. This construction separates the dependence on the large-scale density fluctuations, encoded in $S_{\alpha\beta}$, from the response of the cluster abundance, described by the bias factors in eq. (2.22). In the analysis that follows, this separation allows us to efficiently explore the impact of SSC on cosmological constraints by keeping $S_{\alpha\beta}$ fixed while recomputing the bias-dependent contribution to the covariance, thereby avoiding the need for a full evaluation of the field covariance at each likelihood evaluation. With this covariance model in place, we can now investigate how SSC impacts cosmological constraints derived from cluster number counts.

3 Fiducial Models and Mock Cluster Catalogs

To study the impact of fixing the covariance matrix to a specific cosmological model, we generate mock cluster catalogs assuming a fiducial cosmology, from which cluster redshifts and masses (or mass proxies) are drawn. Since the true cosmological model of the Universe is not known, this controlled setup allows us to quantify the biases and uncertainties that arise when the covariance matrix is evaluated using an incorrect cosmological model. By constructing the mock catalogs consistently from the fiducial model, we are able to directly compare the results obtained when the covariance matrix is computed assuming the correct and incorrect cosmologies.

For the construction of the mock catalogs we follow the hierarchical resampling scheme introduced in Refs. [32, 46] and implemented in NumCosmo [54], to which we refer for the full algorithm. For a given fiducial cosmology, we first draw the binned number counts $N_{i,\alpha}$ from the multivariate Gaussian of eq. (2.18), whose covariance comprises both the Poisson shot-noise and the SSC contributions; the mock counts therefore carry the same super-sample correlations between bins that the likelihood models. Conditional on these counts, the individual cluster properties, mass (or mass proxy) and redshift, are then drawn from the corresponding mass-observable and photometric redshift relations.

The mock catalogs are generated assuming fiducial cosmological models that specify the true underlying properties of dark matter halos. Cluster number counts provide their strongest constraints on the matter density parameter Ω_m ³ and the amplitude of matter fluctuations σ_8 , and, for surveys reaching $z \gtrsim 1.0$, also on the dark energy equation-of-state parameter w . These parameters are therefore allowed to vary over ranges commonly explored in Markov Chain Monte Carlo analyses (in particular, those implemented in NumCosmo). This choice enables us to probe a broad region of cosmological parameter space and to test the robustness of our methodology under different cosmological scenarios.

All remaining cosmological parameters are kept fixed throughout the analyses, namely $H_0 = 67.81$, $n_s = 0.9667$, $\Omega_b = 0.0486$, and massless neutrinos. The adopted parameter values are motivated by the Uchuu simulation suite [62] and the Planck 2018 constraints [49], which assumes a Λ CDM cosmology consistent with the Planck 2018 constraints [49]. The specific combinations of cosmological parameters adopted in each fiducial scenario are presented and discussed in sections 4.1, 4.4, 4.6 and 4.7.

For each fiducial cosmological model, we consider four different experimental setups by varying two survey characteristics that strongly affect cluster number count analyses: the sky coverage and the redshift depth. We adopt survey configurations motivated by current and forthcoming optical surveys. Specifically, we consider an intermediate survey area of $\Omega_{\text{sky}} = 3000 \text{ deg}^2$, characteristic of Stage-III experiments and partial-sky photometric observations, as well as a wide survey covering $\Omega_{\text{sky}} = 18000 \text{ deg}^2$, typical of Stage-IV experiments such as LSST [16]. For each survey area, we explore two redshift ranges, $z \in [0.1, 0.8]$ and $z \in [0.1, 1.5]$, resulting in four survey configurations per fiducial cosmological model.

In addition to the choice of fiducial cosmological parameters, survey area, and redshift depth, we consider different levels of observational realism in the mock catalogs. The first consists of halo catalogs

³In the figures, we denote the present-day value as Ω_{m0} .

with true masses and true redshifts, corresponding to an idealized scenario in which these quantities are perfectly known. The second includes mass proxies while retaining true redshifts, approximating the level of information expected from spectroscopic surveys and from photometric surveys such as J-PAS. The third, and most realistic, case incorporates both mass proxies and photometric redshift estimates, as expected for wide-area photometric surveys such as LSST and Euclid.

For the mass-observable relation, we use eqs. (2.10)–(2.12) assuming: $\mu_0 = 3.207$, $\mu_M = 0.993$, $\mu_z = 0.0$ for the mean $\mu(M, z)$ and $\sigma_0 = 0.456$, $\sigma_M = -0.169$ and $\sigma_z = 0.0$ for the variance $\sigma(M, z)$ taken from [63]. This choice is conservative and broadly consistent with expectations for richness-based mass estimates in photometric surveys. Regarding the photo- z redshift uncertainties, we adopt $\sigma_0^{\text{ph}} = 0.03$ in eq. (2.14), as expected in surveys like LSST [64].

In all cases, i.e., true or photometric redshift, the range in z is divided into seven bins equally spaced, chosen to ensure a sufficient number of clusters per bin and the validity of the Gaussian likelihood approximation. Regarding the true mass, we use a single bin spanning $M \in [10^{14} M_\odot, 10^{15} M_\odot]$. Finally, for the mass-proxy, we consider four equally spaced bins in richness in the range $\lambda \in [20, 200]$.

The complete cluster pipeline is implemented within the NumCosmo framework,⁴ encompassing everything from the background cosmology to the large-scale structure modelling, including the halo mass function, halo bias, the mass-richness relation, photometric redshifts, and cluster count predictions. Furthermore, the likelihood module incorporates a Gaussian likelihood with Super-Sample Covariance (SSC) contributions, alongside a comprehensive suite of statistical tools for Markov Chain Monte Carlo (MCMC) sampling, Monte Carlo simulations, and best-fit optimization.

At the time the results presented in this work were produced, the computation of the S matrix used to determine the covariance of the background matter distribution was performed externally using the PySSC package developed in [31].⁵ We note, however, that a dedicated SSC module has since been implemented within NumCosmo, providing functionality equivalent to that of PySSC. This module is currently in a validation phase and will be described in a forthcoming publication (Vitenti et al., in preparation).

4 Analyses and Results

In a realistic cluster analysis the cosmology is unknown, yet the covariance matrix must be specified to evaluate the likelihood. Because the SSC term is expensive, the covariance (or parts of it) is often built at a single fiducial cosmology and held fixed while the cosmological parameters are sampled. The question we address is how this approximation propagates into the inferred parameters: does it bias the estimators, and does it distort the reported uncertainties?

To answer this in a controlled way, we fix a single fiducial cosmology,

$$(\Omega_{m0}, \sigma_8, w) = (0.3098, 0.8159, -1.0), \quad (4.1)$$

together with the remaining parameters of section 3,⁶ and generate *one* mock data vector per survey configuration. As described in section 3, we consider the four survey layouts spanned by $\Omega_{\text{sky}} \in \{3000, 18000\} \text{ deg}^2$ and $z_{\text{max}} \in \{0.8, 1.5\}$.

We study covariance misspecification in two complementary configurations. In the *forward* configuration the mock is held at the fiducial cosmology and the same data vector is re-analysed under several constructions of the covariance matrix, displaced to other cosmologies and labelled in section 4.1; because the data vector is fixed, any change in the inferred posterior is attributable solely to the covariance choice. In the *mirror* configuration the converse holds, as in a real analysis: the covariance is fixed at the fiducial

⁴<https://github.com/NumCosmo/NumCosmo>

⁵<https://pyssc.readthedocs.io/>

⁶The sampled density parameter is the cold dark matter density $\Omega_c = 0.2612$; throughout we quote the total matter density $\Omega_{m0} = \Omega_c + \Omega_b = 0.3098$.

value while the mock is generated at a displaced cosmology, so that the data correspond to the unknown true one and the covariance to an assumed cosmology. Since the impact of covariance misspecification should depend only on the mismatch between the data and covariance cosmologies, not on which of the two is displaced, we expect the two configurations to probe the same effect; we test this explicitly in section 4.3. We use these labels, *forward* and *mirror*, throughout.

We organise the study in two stages. We first map the effect on the posterior *width* using individual MCMC runs. In section 4.1 we vary how the covariance is built on a fixed (*forward*) mock, isolating the role of the SSC S matrix, of the full covariance, and of the shot-noise-only limit. In section 4.2 we verify that shifting two cosmological parameters simultaneously produces no effect beyond the sum of the individual shifts. In section 4.3 we show that the realistic *mirror* configuration reproduces the *forward* results once both are placed on a common cosmology-mismatch axis. We then turn, in section 4.4, to a Monte Carlo (MC) ensemble to show that covariance misspecification does not add any detectable bias to the parameter *estimators*, so that its effect is confined to the parameter *uncertainties*. In section 4.5 we verify that these results are robust to a realistic mass proxy and to LSST-like photometric redshifts. The consequences for the σ_8/S_8 tension and a practical mitigation strategy are discussed in sections 4.6 and 4.7. Altogether, the systematic campaign underlying sections 4.1–4.5 comprises of order 400 complete MCMC analyses and more than 3×10^4 best-fit Monte Carlo realizations.

Throughout, we quantify the impact of a covariance choice on a parameter $\theta \in \{\Omega_{m0}, \sigma_8, w\}$ through the ratio of its marginal posterior width to the width obtained when the covariance is built consistently at the true (fiducial) cosmology,

$$R_\theta \equiv \frac{\sigma_\theta}{\sigma_\theta^{\text{match}}}, \quad \Delta_\theta \equiv 100 (R_\theta - 1) [\%], \quad (4.2)$$

where the reference analysis (MATCH, defined in section 4.1) uses the covariance evaluated at the same cosmology that generated the mock. By construction $R_\theta = 1$ for the reference (MATCH); $R_\theta < 1$ (> 1) signals an under- (over-)estimated uncertainty.

4.1 Covariance choices on a fixed mock

For each survey layout we re-analyse the fiducial mock with the covariance C of the Gaussian likelihood (eq. (2.18)) built in one of three ways, which we label and use throughout:

S-FIX only the SSC kernel S (eq. (2.27)) is held fixed, while the bias and number-count prefactors $b_{i\alpha}\bar{\mu}_{i\alpha}$ (eq. (2.22)) are recomputed at every MCMC step. This mirrors the practical strategy of freezing only the expensive S matrix.

FULL-FIX the entire matrix C (shot noise, counts, bias and S) is fixed.

NO-SSC the SSC term is dropped, retaining only the Poisson shot noise (eq. (2.21)).

For S-FIX and FULL-FIX, the frozen ingredients are evaluated either at the true fiducial cosmology or at a displaced one. We define “match” as the analysis performed with the covariance built at the true cosmology; this sets the reference width $\sigma_\theta^{\text{match}}$ of eq. (4.2), at which S-FIX and FULL-FIX coincide. Rather than probing only a few extreme values in parameter space, we scan each parameter independently over a sequence of displacements,

$$\Delta\Omega_{m0} \in \{\pm 0.01, \pm 0.03, \pm 0.06\}, \quad \Delta w \in \{\pm 0.05, \pm 0.10, \pm 0.20, \pm 0.40\}, \quad \Delta\sigma_8 \in \{\pm 0.02, \pm 0.05, \pm 0.10\}, \quad (4.3)$$

and repeat the scan for both S-FIX and FULL-FIX. Each curve in figure 1 is therefore traced by 7–9 independent MCMC analyses of the same mock realization: we run a full MCMC for every shift in θ , covariance construction (where applicable), and survey layout, rather than interpolating between a few

points. Together with the baselines, this scan comprises 176 complete MCMC analyses across the four survey layouts, using our default of seven redshift bins (section 3). Repeating the scan with a finer binning of fourteen redshift bins for the deeper $z_{\max} = 1.5$ layouts as a robustness check brings the single-parameter total to 264 runs.

Unless stated otherwise, we quote results for the configuration in which covariance misspecification has the largest effect on the parameters, $\Omega_{\text{sky}} = 18000, \text{deg}^2$ and $z_{\max} = 0.8$. The full scan over all four layouts is shown in figure 1. The size of the effect reflects the contribution of the SSC term relative to the Poisson shot noise: it is largest for the widest footprint, which couples most strongly to super-survey modes, and depends only weakly on depth, marginally favouring the shallower survey, whose smaller comoving volume carries a somewhat larger super-sample variance. Because the cosmology dependence of the covariance enters almost entirely through the SSC term, this configuration maximises the impact of covariance misspecification, and the quoted results bound the effect across the layouts we consider.

Each of these 264 configurations is a *complete* MCMC analysis, not a Fisher estimate: we use the APES sampler [65] with 500 walkers and 120 steps (6×10^4 samples per run). The chains converge within ~ 30 – 40 steps, and we conservatively discard the first 50 steps (2.5×10^4 samples) as burn-in before computing posterior statistics. Across the *entire* scan, over every displacement on θ , layout and covariance construction, the location of the posterior is remarkably stable: the recovered means depart from the reference analysis (MATCH) by at most $\sim 1\%$ (largest for w , and well below 0.5% for Ω_{m0} and σ_8), and even in the most degenerate configurations this displacement remains negligible compared with the parameter uncertainty ($\ll 1\sigma$). Covariance misspecification thus leaves the inferred parameters essentially unchanged and acts almost entirely on the *width* of the posterior. We therefore characterise the effect through the width ratio R_θ in the remainder of this section, and confirm over an ensemble of realizations that covariance misspecification adds no detectable bias in section 4.4.

Under FULL-FIX at the true cosmology the posterior widths are indistinguishable from MATCH, $R_\theta = 1.00$ for all parameters and layouts. Fixing the covariance is therefore not, by itself, the source of error: the error arises only when it is fixed at the *wrong* (displaced) cosmology.

Under S-FIX at a displaced cosmology, with the bias and counts still recomputed during sampling, the widths change only mildly. Even for the largest displacements we find $|\Delta_\theta| \lesssim 6\%$ for σ_8 ($R_{\sigma_8} = 0.95$ at $\Delta\sigma_8 = -0.10$, 1.06 at $+0.10$), and $\lesssim 12\%$ for the most extreme Ω_{m0} displacement. Since the S matrix is the computationally expensive ingredient, this is a positive practical result: fixing it at an approximate cosmology, provided the cheap counts and bias are kept consistent, has a minor impact on the inferred uncertainties.

Under FULL-FIX at a displaced cosmology, by contrast, the widths distort substantially. For σ_8 we find $R_{\sigma_8} = 0.63$ at $\Delta\sigma_8 = -0.10$ and $R_{\sigma_8} = 1.37$ at $+0.10$, a $\pm 37\%$ mis-estimation, with a monotonic dependence on the displacement. The effect is controlled by the amplitude of matter fluctuations: a covariance built at a *lower* amplitude underestimates the true variance and yields artificially tight posteriors ($R < 1$), while a higher amplitude broadens them ($R > 1$). Displacements in Ω_{m0} and w act in the same, weaker, sense ($R_{\sigma_8} \in [0.88, 1.10]$ for $\Delta\Omega_{m0} = \pm 0.06$; $[0.87, 1.08]$ for $\Delta w = \pm 0.40$).

The contrast between S-FIX and FULL-FIX is informative. Their difference is precisely whether the bias and count prefactors $b_{i\alpha}\bar{\mu}_{i\alpha}$ are recomputed or fixed. The fact that S-FIX is nearly harmless while FULL-FIX is not shows that the dominant cosmology dependence of the cluster-count covariance resides in the abundance and bias prefactors, not in the S matrix itself. This is physically expected: the cluster abundance is exponentially sensitive to the fluctuation amplitude, so holding $b\bar{\mu}$ fixed at a wrong amplitude strongly mis-scales the SSC term, whereas S varies comparatively slowly with cosmology.

The NO-SSC construction underestimates the uncertainties by an amount that grows strongly with survey area. For $\Omega_{\text{sky}} = 18000 \text{deg}^2$ we find $R_{\sigma_8} \simeq 0.77$ – 0.79 (a $\sim 25\%$ underestimation of the σ_8 error), falling to $R_{\sigma_8} \simeq 0.94$ – 0.95 (a $\sim 5\%$ effect) at 3000deg^2 . The dependence on z_{\max} is comparatively weak. The same area ordering holds for all the covariance-misspecification effects discussed above, consistent with the SSC term carrying progressively more weight as the footprint grows.

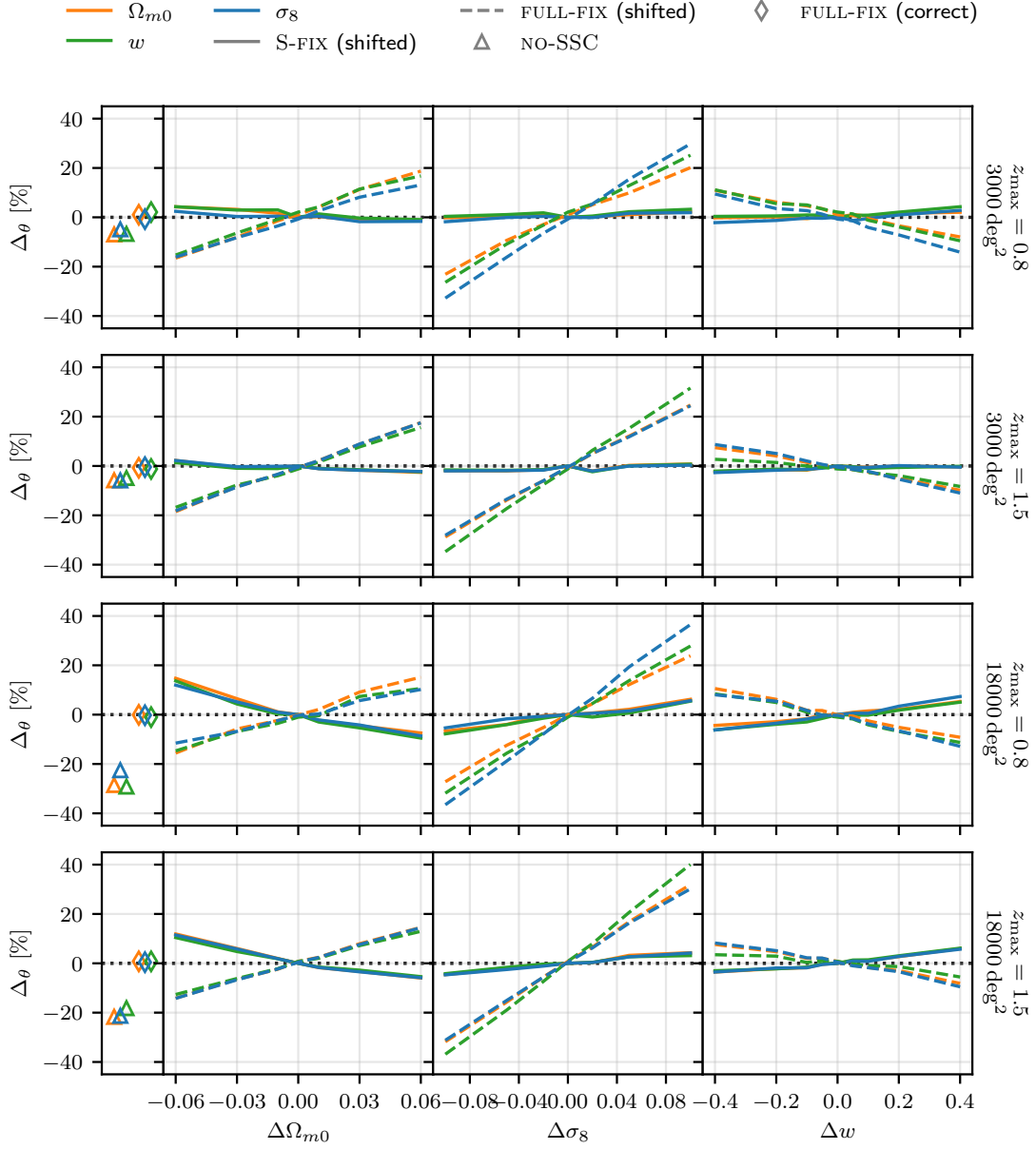


Figure 1: Relative change in the marginal posterior width, $\Delta_\theta = 100(\sigma_\theta/\sigma_\theta^{\text{match}} - 1)$, for $\theta \in \{\Omega_{m0}, \sigma_8, w\}$ as the covariance is displaced from the true fiducial cosmology. Rows are survey layouts ($\Omega_{\text{sky}} \times z_{\text{max}}$); the leftmost (narrow) column shows the layout-dependent baselines (NO-SSC, triangles; FULL-FIX at the correct cosmology, diamonds), and the remaining columns show the single-parameter scans in Ω_{m0} , σ_8 and w . Each curve is sampled at the displacements of eq. (4.3) (7–9 points). Solid curves (S-FIX) fix only the S matrix at the displaced cosmology and stay close to zero; dashed curves (FULL-FIX) freeze the full covariance and produce a large, monotonic, amplitude-driven distortion.

Figure 2 shows these effects directly for two representative cases, overlaying the posterior of $(\Omega_{m0}, \sigma_8, w)$ from the same mock under MATCH, S-FIX at $\Delta\sigma_8 = \pm 0.10$, and FULL-FIX at the same displaced cosmologies. The S-FIX posteriors (left panel) are essentially identical to MATCH, whereas the FULL-FIX ones (right panel) are visibly broadened or narrowed depending on the sign of the covariance mismatch; all five share the same location, marked by the fiducial values (consistent with the absence of bias established in section 4.4 but with a natural statistical shift). The figure therefore illustrates the central result of this section: covariance misspecification affects primarily the size and shape of the credible regions rather than the location of the posterior maximum.

Figure 3 presents the analogous comparison for covariance mismatches generated by displacing Ω_{m0} . In contrast to the σ_8 case, the impact of covariance misspecification is of comparable magnitude for the S-FIX and FULL-FIX prescriptions, but with opposite trends: a displacement that broadens the posterior in one prescription narrows it in the other. Together, figures 2 and 3 provide the full posterior view of the behaviour quantified in figure 1, showing how the changes in variance ratios translate into the geometry of the multidimensional credible regions.

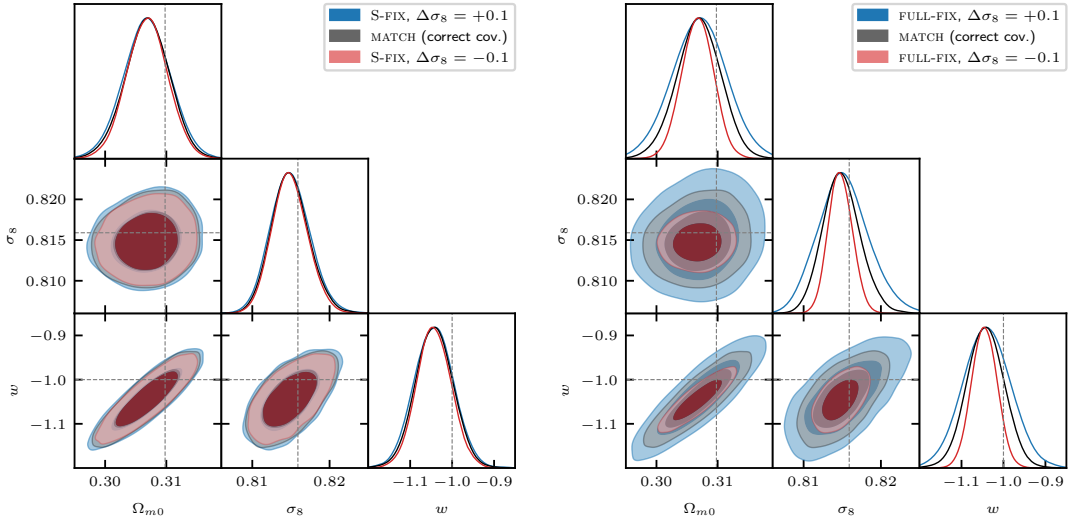


Figure 2: Posterior constraints on $(\Omega_{m0}, \sigma_8, w)$ from a single mock realization for the most sensitive survey configuration ($\Omega_{\text{sky}} = 18000, \text{deg}^2, z_{\text{max}} = 0.8$). The left panel compares the reference analysis (MATCH, black) with analyses in which only the S matrix is fixed at cosmologies with $\Delta\sigma_8 = \pm 0.10$ (red and blue). The right panel shows the corresponding comparison when the entire covariance is fixed at those displaced cosmologies. Contours denote the 68% and 95% credible regions, and dashed lines indicate the fiducial parameter values. Both panels are plotted using identical parameter ranges, allowing a direct comparison of posterior widths. Fixing only S has a negligible impact on the inferred constraints, with contours nearly coincident with the reference result. In contrast, fixing the full covariance produces a substantially larger change in the posterior volume, broadening or narrowing the constraints depending on the sign of the covariance mismatch, while leaving the posterior centre essentially unchanged.

While the per-parameter ratios R_θ summarise the marginal widths, it is useful to also quote a single joint figure of merit. For this we use the volume of the highest-posterior-density (HPD) credible region in the three-dimensional $(\Omega_{m0}, \sigma_8, w)$ space, that is, the smallest region enclosing a fixed fraction α of the posterior; we take $\alpha = 0.6827$ (the 68% region), so that a smaller volume corresponds to a tighter joint constraint. We estimate it directly from the MCMC chain with the procedure implemented in NumCosmo,

which selects the α fraction of samples with the highest posterior probability and evaluates the enclosed parameter-space volume (appendix A). Denoting this volume V , we report its change relative to the `MATCH` analysis, $\Delta V/V_{\text{match}}$. Being a joint measure, V is complementary to the marginals in two respects. First, it compounds the individual width changes: for a Gaussian posterior $V = (\prod_i \sigma_i) \sqrt{\det R}$, with R the correlation matrix, so $\Delta V/V$ is of the order of the sum of the per-parameter Δ_θ and is therefore much larger than any single one. For `FULL-FIX` at $\Delta\sigma_8 = +0.10$ (worst-case layout) the credible volume more than doubles ($\Delta V/V_{\text{match}} \simeq +130\%$), against the $\sim 37\%$ change of the σ_8 marginal alone; at $\Delta\sigma_8 = -0.10$ it shrinks by $\sim 67\%$, while `S-FIX` remains mild ($\simeq +17\%$). Second, and unlike the R_θ , V responds to changes in the correlation structure R itself. Figure 4 isolates this contribution: the solid curve is $\Delta V/V$ and the dashed curve is the product of the marginal width ratios, that is, the value V would take if the correlations were unchanged; the shaded difference between them is the effect of the shifting degeneracy directions. A fixed covariance therefore misestimates not only the size of the confidence region but also its shape, an effect that only a joint measure such as V makes explicit.

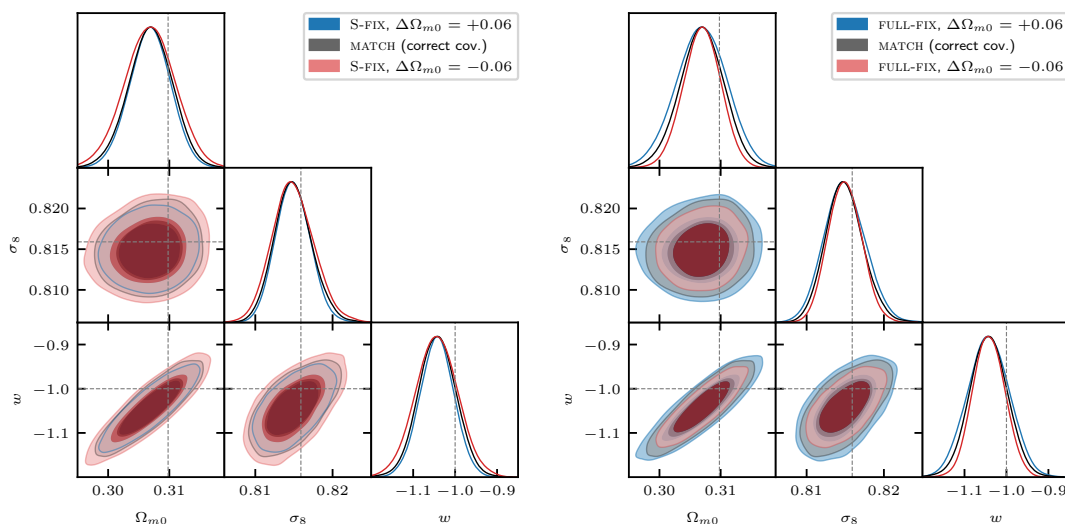


Figure 3: Same as figure 2, but for covariance mismatches generated by displacing the fiducial matter density by $\Delta\Omega_{m0} = \pm 0.06$. The left panel compares the `S-FIX` prescription, in which only the S matrix is fixed at the displaced cosmology, while the right panel shows the `FULL-FIX` prescription, in which the entire covariance is fixed. Black contours correspond to the reference (`MATCH`) analysis, and red and blue contours to positive and negative parameter displacements, respectively. Contours denote the 68% and 95% credible regions, dashed lines indicate the fiducial parameter values, and both panels use identical parameter ranges. In contrast to figure 2, the impact of covariance misspecification is of comparable magnitude for the `S-FIX` and `FULL-FIX` prescriptions, but with opposite trends: positive and negative displacements broaden different sides of the comparison. This reflects, in the full posterior distribution, the same behaviour observed in figure 1.

4.2 Combined parameter shifts

The analysis above displaces one parameter at a time. To check for non-linear interactions, we repeat it for simultaneous two-parameter displacements (in $\Omega_{m0} \times w$, $\Omega_{m0} \times \sigma_8$ and $w \times \sigma_8$) at the worst-case layout, under both `S-FIX` and `FULL-FIX`, for a total of 24 MCMC analyses. In every case the combined effect equals the sum of the individual effects to within the realization noise: for example,

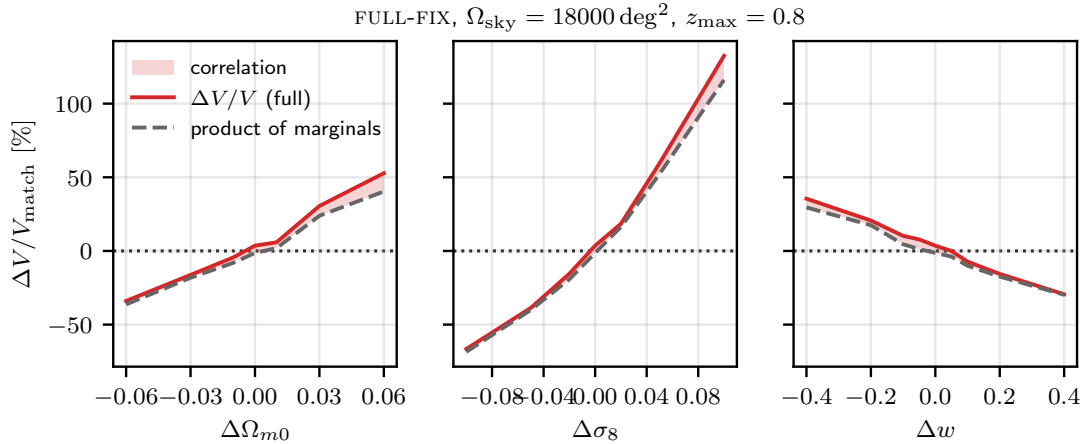


Figure 4: Joint 68% credible-volume change $\Delta V/V_{\text{match}}$ at the worst-case layout ($\Omega_{\text{sky}} = 18000 \text{ deg}^2$, $z_{\text{max}} = 0.8$) with the full covariance fixed at a displaced cosmology, as a function of the displacement in Ω_{m0} , σ_8 and w . The solid curve is the joint volume; the dashed curve is the product of the three marginal width ratios (the value expected if the correlations were unchanged). The shaded gap is the contribution of the altered correlation/degeneracy structure, which the per-parameter widths do not capture.

$(\Delta\Omega_{m0}, \Delta\sigma_8) = (+0.03, +0.05)$ yields $\Delta\sigma_8 = +22.9\%$ against a sum of individual shifts of $+25.0\%$, and $(\Delta w, \Delta\sigma_8) = (-0.10, -0.05)$ yields -17.7% against -17.1% . No non-linear coupling between parameters is detected, so the single-parameter sweeps of section 4.1 fully characterise the behaviour over the relevant region of parameter space. Figure 5 makes this explicit: the combined-shift width change tracks the sum of the corresponding single-shift changes along the identity line for all parameters and for both S-FIX and FULL-FIX.

4.3 Forward and mirror configurations agree

The *forward* runs of the preceding sections hold the mock at the fiducial cosmology and displace the covariance, whereas a real analysis is the *mirror* of this. To show that the two are equivalent, we reanalyse the worst-case layout in the *mirror* configuration, generating the mock at a displaced cosmology ($\Delta\Omega_{m0} = \pm 0.03$, $\Delta\sigma_8 = \pm 0.05$, $\Delta w = \pm 0.10$) and fitting it with the covariance held at the fiducial value, under both S-FIX and FULL-FIX. With the matching correct-covariance analyses at each displaced cosmology, this amounts to 24 MCMC analyses. Each *mirror* run is normalised to its own MATCH reference, the analysis with the covariance built consistently at that displaced cosmology, so that $\Delta\theta$ again measures the misspecified width against the correct one.

The key observation is that what drives the effect is the signed mismatch between the covariance and the data cosmologies, $\delta\theta \equiv \theta_{\text{cov}} - \theta_{\text{data}}$, where θ_{data} is the cosmology used to generate the mock and θ_{cov} the cosmology at which the frozen part of the covariance (the full matrix under FULL-FIX, the S matrix alone under S-FIX) is evaluated. In the *forward* sweep a covariance displaced by $+s$ on fiducial data gives $\delta\theta = +s$; in the *mirror* runs a covariance held at the fiducial value while the data move by $+t$ gives $\delta\theta = -t$. Placing both on this common axis, figure 6 shows the *mirror* points falling onto the *forward* curves for every inferred parameter and for both covariance constructions. For instance, freezing the full covariance under a σ_8 mismatch of $+0.05$ inflates σ_{σ_8} by $+20\%$ in the *forward* sweep and by $+24\%$ in the *mirror* run, while S-FIX leaves it within a few percent in both cases; the residual differences are consistent with the realization noise of single mocks. The impact of covariance misspecification therefore depends only

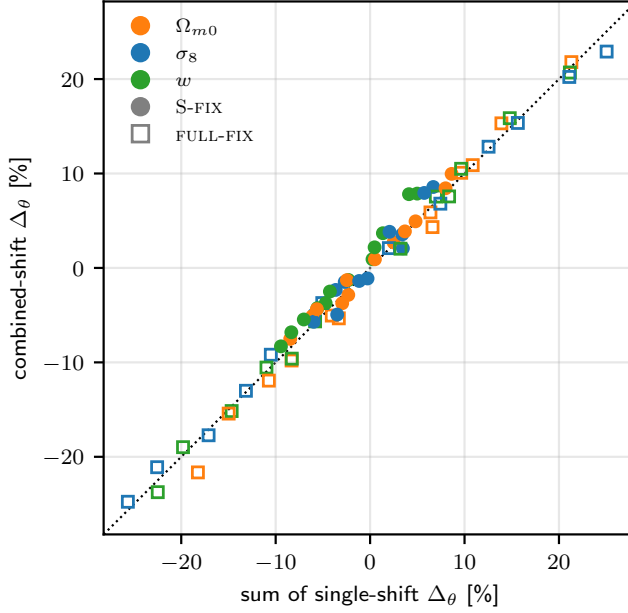


Figure 5: Test for non-linear parameter coupling at the worst-case layout ($\Omega_{\text{sky}} = 18000 \text{ deg}^2$, $z_{\text{max}} = 0.8$). For each two-parameter shift, the combined width change $\Delta\theta$ is plotted against the sum of the two single-parameter changes, for Ω_{m0} , σ_8 and w and for S-FIX (filled) and FULL-FIX (open). Points follow the identity line (dotted), confirming that the shifts superpose linearly.

on the cosmology mismatch and not on which of the data or the covariance is displaced, so the *forward* scan of section 4.1 is representative of a real analysis.

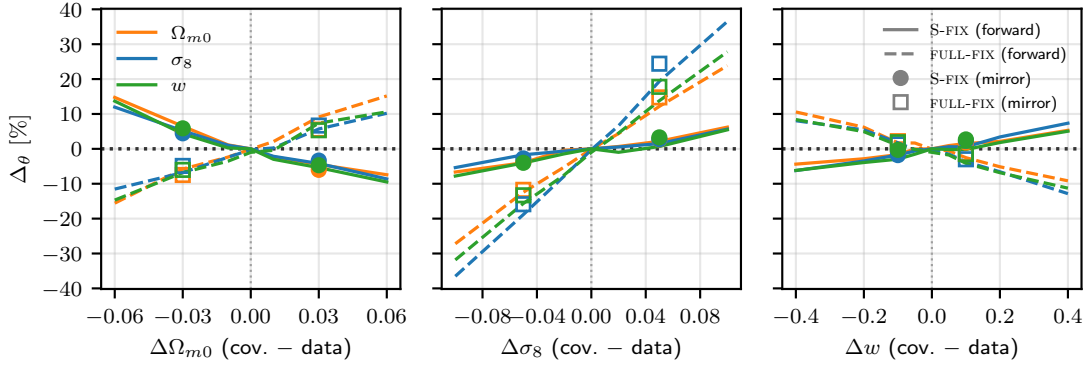


Figure 6: Equivalence of the forward and mirror configurations at the worst-case layout ($\Omega_{\text{sky}} = 18000 \text{ deg}^2$, $z_{\text{max}} = 0.8$), shown on a common cosmology-mismatch axis $\delta\theta = \theta_{\text{cov}} - \theta_{\text{data}}$. Curves are the forward single-parameter sweeps (solid: S-FIX; dashed: FULL-FIX); markers are the mirror runs (filled circles: S-FIX; open squares: FULL-FIX), generated at a displaced cosmology and plotted at $\delta\theta = -\text{shift}$. Colours denote the inferred parameter. The mirror points lie on the forward curves, confirming that the effect is set by the data-covariance mismatch alone.

4.4 Bias of the parameter estimators

The results above concern the *width* of the posterior on a single realization; we now turn to the *location* of the estimators. Point estimators such as the posterior mean, or equivalently the maximum-likelihood estimate, are in general only *asymptotically* unbiased: at finite data they can carry an intrinsic bias that is present even when the covariance is built correctly, and covariance misspecification could in principle add to it. The relevant question is therefore not whether the estimators are exactly unbiased, but whether misspecifying the covariance *introduces* a bias beyond the intrinsic one. To answer it we measure the *total* estimator bias in each configuration and include, as a control, the correct-covariance case with no cosmology shift, against which the misspecified cases can be compared.

We perform a Monte Carlo study at the worst-case layout, drawing $N = 1000$ independent mock catalogs per configuration and recording the best fit of each. The configurations are arranged so that every misspecified analysis can be compared against a correctly specified one *at the same true cosmology*. In the *forward* configuration the mocks are generated at the fiducial cosmology and analysed either with the correct covariance (MATCH) or with the SSC term dropped (NO-SSC). In the *mirror* configuration the mocks are generated at each displaced cosmology and analysed either with the covariance rebuilt consistently at that same cosmology (the correct, MATCH, analysis) or with the covariance held at the fiducial value (the misspecified analysis, which is the realistic one). Each of these is run for both freezings, S-FIX and FULL-FIX. This yields two groups: a *correct-covariance* control (the forward MATCH run and the mirror runs analysed at their own cosmology) and a *misspecified* set (the forward NO-SSC run and the mirror runs analysed with the covariance fixed at the fiducial value). Comparing the two groups at matched true cosmology isolates any bias introduced by misspecification from the intrinsic finite-sample bias common to both. In total this covers 28 covariance configurations, each resampled $N = 1000$ times, for 28,000 independent best-fit analyses.

For each mock we record $\hat{\theta}$, the best-fit (point) estimate of the parameter θ returned by the fit. We define the estimator bias as $\text{Bias}(\hat{\theta}) = \langle \hat{\theta} \rangle - \theta_{\text{true}}$, where $\langle \hat{\theta} \rangle$ is the mean of $\hat{\theta}$ over the ensemble and θ_{true} is the value of that parameter used to generate the mocks, that is, the resample cosmology at which the catalogs are drawn. We quote the bias in units of the per-realization scatter σ_{θ} , the standard deviation of $\hat{\theta}$ across the ensemble. Since $\langle \hat{\theta} \rangle$ is the mean of N independent estimates, its standard error is σ_{θ}/\sqrt{N} , so the ensemble resolves a bias only down to $1/\sqrt{N} \approx 0.03 \sigma$; under the null hypothesis of no bias, $\text{Bias}(\hat{\theta})/\sigma_{\theta}$ has standard deviation $1/\sqrt{N}$ and should fall within $\pm 2/\sqrt{N}$, two standard errors of the mean, about 95% of the time.

No bias is resolved in any configuration, and crucially none is added by misspecifying the covariance (figure 7). Already the correct-covariance controls carry $|\text{Bias}(\hat{\theta})| \lesssim 0.1 \sigma$ (typically $\lesssim 0.07 \sigma$; in absolute terms $10^{-5} \lesssim |\text{Bias}(\hat{\theta})| \lesssim 10^{-3}$), consistent with zero to within about 0.1σ . The misspecified set scatters within the same band and is statistically indistinguishable from the controls at the matched true cosmology, whether the covariance is stripped of its SSC term on a fiducial mock (*forward* NO-SSC) or held at the fiducial value while the data are displaced (the realistic *mirror* case of section 4.3). Of the roughly eighty parameter estimates only a handful stray marginally beyond the $\pm 2/\sqrt{N}$ band, consistent with the one-in-twenty rate expected for a 95% interval, and with no systematic trend with the shift. The residual is not entirely random, however: across the ensembles σ_8 is recovered marginally high and Ω_{m0} marginally low (mean biases $+0.06 \sigma$ and -0.02σ , of consistent sign across the configurations), the opposite signs tracing the $\Omega_{m0}-\sigma_8$ anti-correlation, i.e. a small displacement along the degeneracy direction. This coherent offset is the intrinsic finite-sample bias of the estimator: it stays below 0.1σ and, crucially, is the same in the correct-covariance controls as in the misspecified configurations, so it is not induced by the covariance choice. Covariance misspecification therefore adds no detectable bias; its effect is confined to the inferred uncertainties, as quantified in section 4.1, not the location of the recovered parameters. The Monte Carlo ensemble also provides a second reading of the credible volume of section 4.1: the covariance volume of the best-fit ensemble, computed as $\sqrt{\det \text{Cov}}$ over the $N = 1000$ best fits, agrees with the HPD volume of the corresponding MCMC posterior. The same joint volume

can thus be obtained either from the posterior chains or from the ensemble of estimators (appendix A), confirming that the volume estimates used in this work faithfully represent the statistical scatter of the estimators.

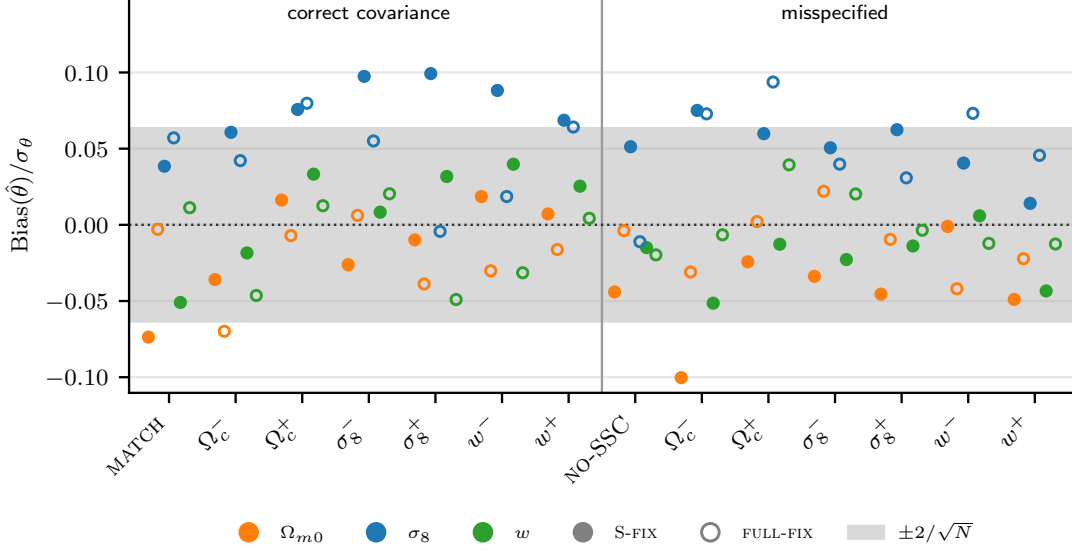


Figure 7: Estimator bias in units of the parameter scatter, $\text{Bias}(\hat{\theta})/\sigma_{\theta}$, from the $N = 1000$ Monte Carlo ensemble at the worst-case layout ($\Omega_{\text{sky}} = 18000 \text{ deg}^2$, $z_{\text{max}} = 0.8$). Colour denotes the inferred parameter (Ω_{m0} , σ_8 , w) and the marker fill the covariance freezing (filled: S-FIX; open: FULL-FIX); each column is one configuration. Columns are split into the *correct-covariance* control, where the covariance is built at the cosmology that generated the mock, and the *misspecified* set. The control comprises the *forward* MATCH run (mock and covariance at the fiducial cosmology) and the *mirror* runs at each shift (mock at the displaced cosmology, covariance rebuilt there). The misspecified set comprises the *forward* NO-SSC run (SSC term dropped on a fiducial mock) and the *mirror* runs at each shift with the covariance held at the fiducial value (Ω_c , σ_8 , w shifted by \pm), the realistic case. The shaded band is $\pm 2/\sqrt{N}$, two standard errors of the ensemble mean (about 95% C.L.) expected for an unbiased estimator. The two groups scatter parameters identically within the band, showing that covariance misspecification does not displace the recovered parameters.

4.5 Observational realism: mass proxy and photometric redshifts

The analyses so far use idealised catalogs with true masses and redshifts. We now repeat the worst-case forward sweep with two more realistic catalog constructions (section 3): *mp*, which replaces the true mass by the richness through the mass-observable relation (four richness bins over $\lambda \in [20, 200]$), and *mpz*, which additionally replaces the true redshift by a Gaussian photometric estimate with an LSST-like scatter $\sigma_0^{\text{ph}} = 0.03$. Each realism level is analysed against its own MATCH reference, so the width ratios continue to isolate the covariance choice. Each level follows the worst-case single-parameter sweep of section 4.1 under both freezings (44 MCMC analyses) together with the match-family Monte Carlo (4,000 best fits).

Adding observational scatter degrades the constraints, as expected. Table 1 lists the absolute marginal 1σ errors of the correctly-specified analysis: at the true cosmology σ_8 is constrained to 0.30%, Ω_{m0} to 1.2% and w to 4.5% for idealised catalogs, degrading to 0.41%, 1.6% and 5.3% for *mp* and to 0.41%,

1.7% and 5.7% for mpz . In other words the widths broaden by 38%–39% on Ω_{m0} and σ_8 and by 18% on w for mp , and by 49%, 39% and 26% for mpz : the realistic photo-z scatter adds little to the marginal σ_8 constraint beyond the mass proxy, and only a modest amount on Ω_{m0} and w . Figure 8 shows the same posteriors in the $(\Omega_{m0}, \sigma_8, w)$ planes: the contours broaden from *true* to mp to mpz while preserving their orientation and remaining centred on the fiducial, with mpz only marginally wider than mp . The recovered means lie within the single-realization scatter ($\leq 1\sigma$) of the fiducial at every realism level, consistent with the unbiasedness established in section 4.4.

Table 1: Marginal 1σ constraints (posterior standard deviations) from the correctly-specified (MATCH) analysis at the worst-case layout ($\Omega_{\text{sky}} = 18000 \text{ deg}^2$, $z_{\text{max}} = 0.8$), for the three realism levels: true masses and redshifts, mass proxy (mp), and mass proxy plus LSST-like photo-z (mpz). Values in parentheses are the fractional constraint $\sigma_\theta/|\theta_{\text{fid}}|$, with $(\Omega_{m0}, \sigma_8, w)_{\text{fid}} = (0.3098, 0.8159, -1)$.

Parameter	true	mp	mpz
$\sigma_{\Omega_{m0}}$	0.0036 (1.2%)	0.0050 (1.6%)	0.0054 (1.7%)
σ_{σ_8}	0.0024 (0.30%)	0.0034 (0.41%)	0.0034 (0.41%)
σ_w	0.045 (4.5%)	0.053 (5.3%)	0.056 (5.7%)

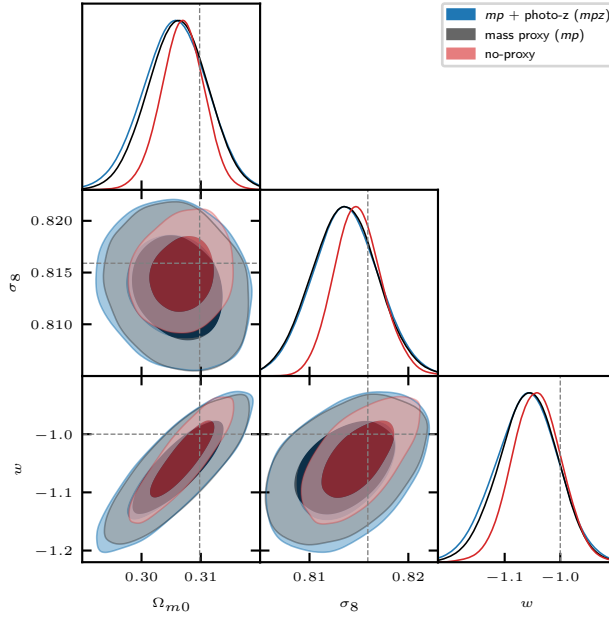


Figure 8: Correctly-specified (MATCH) posterior of $(\Omega_{m0}, \sigma_8, w)$ at the worst-case layout for the three realism levels: true masses and redshifts (no-proxy, red), mass proxy (mp , grey), and mass proxy plus LSST-like photo-z (mpz , blue). Contours are the 68% and 95% credible regions; dashed lines mark the fiducial values. The constraints broaden with realism while preserving their orientation and staying centred on the fiducial; mpz is barely wider than mp , confirming that LSST-like photo-z adds little beyond the mass proxy.

The impact of covariance misspecification, by contrast, is essentially unchanged across realism (figure 10). The dominant FULL-FIX distortion persists at both proxy levels: at $\Delta\sigma_8 = +0.10$ (-0.10) the

σ_8 width is mis-estimated by +37% (−37%) for true masses, +34% (−32%) for mp and +35% (−32%) for mpz , and the joint credible volume roughly doubles in every case ($\Delta V/V_{\text{match}} \simeq +124\%$, +119%, +123% at $\Delta\sigma_8 = +0.10$) and shrinks to roughly half its size (with particular cases going up to 37% of the fiducial volume) at $\Delta\sigma_8 = -0.10$. The S-FIX construction remains benign across all realism levels ($|\Delta\theta| \lesssim 4\%$). The only qualitative change is in the NO-SSC limit, whose underestimation shrinks markedly with realism: the σ_8 (Ω_{m0}) error is underestimated by 23% (28%) for true masses but only by $\sim 3\%$ ($\sim 11\%$) at both mp and mpz . This is consistent with the physical picture of section 4.1: observational scatter raises the shot-noise floor and so lowers the relative weight of the SSC term, which makes dropping or freezing S less consequential, while the FULL-FIX effect, driven by the abundance and bias prefactors rather than by S , is essentially realism-independent.

The estimator-bias study of section 4.4, repeated at the mp and mpz realism levels (the match-family controls, $N = 1000$ each), confirms that the estimators remain unbiased there as well (figure 9): all biases stay below 0.07σ , and the same small intrinsic offset noted in section 4.4, with σ_8 recovered marginally high and Ω_{m0} marginally low, persists unchanged across realism. The results obtained with idealised catalogs are therefore robust to a realistic mass proxy and to LSST-like photometric redshifts.

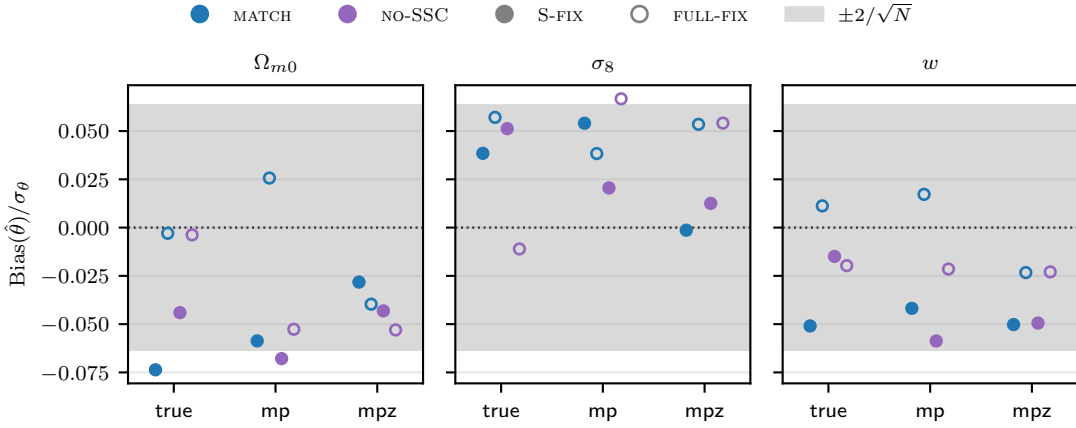


Figure 9: Estimator bias in units of the parameter scatter, $\text{Bias}(\hat{\theta})/\sigma_\theta$, from the $N = 1000$ Monte Carlo across the three realism levels (true masses and redshifts; mass proxy, mp ; mass proxy plus LSST-like photo- z , mpz) at the worst-case layout ($\Omega_{\text{sky}} = 18000 \text{ deg}^2$, $z_{\text{max}} = 0.8$). Each panel is an inferred parameter; within each realism the forward match-family controls are shown, MATCH (correct covariance) and NO-SSC, each for the S-FIX (filled) and FULL-FIX (open) freezings. The shaded band is $\pm 2/\sqrt{N}$, two standard errors of the mean ($\sim 95\%$ C.L.). All points lie within the band at every realism level, and the small intrinsic offset (σ_8 high, Ω_{m0} low) is the same as for true masses, so observational realism neither introduces nor amplifies an estimator bias. The proxy Monte Carlo covers the forward match family only; the shifted cases are covered for true masses in figure 7.

4.6 S_8 tension

Building on the preceding sections, where the parameter estimators are unbiased (section 4.4) while the posterior widths are mis-estimated by tens of per cent (section 4.1), we now examine the consequences for the S_8 tension between cluster counts and early-time probes.

Because covariance misspecification leaves the recovered parameters in place and acts only on their uncertainties, it cannot create or move a tension; it rescales the tension’s *statistical significance*. The relevant axis is $S_8 \equiv \sigma_8 \sqrt{\Omega_m/0.3}$, which lies approximately orthogonal to the principal (Ω_m, σ_8)

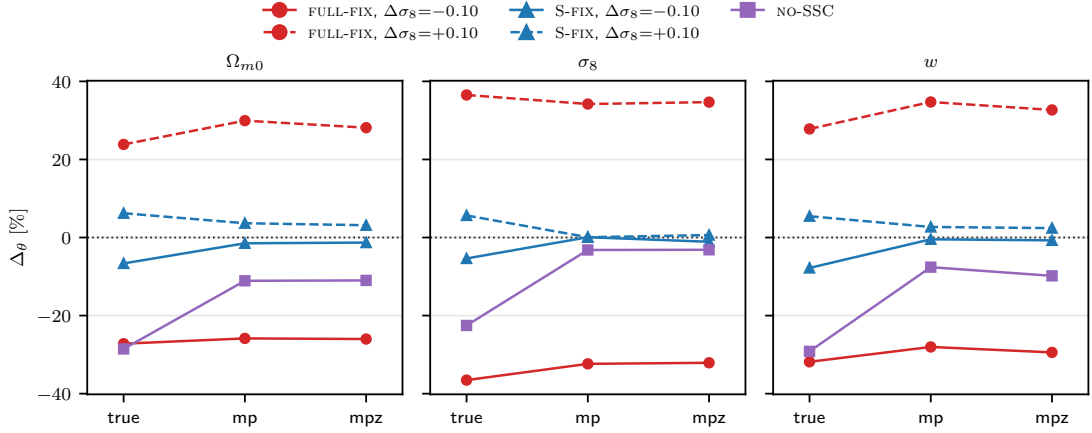


Figure 10: Robustness of the covariance-misspecification effect to observational realism at the worst-case layout ($\Omega_{\text{sky}} = 18000 \text{ deg}^2$, $z_{\text{max}} = 0.8$). Each panel is an inferred parameter; each line is a covariance choice, with the width change $\Delta_\theta = 100(\sigma_\theta/\sigma_\theta^{\text{match}} - 1)$ plotted against the realism level (true masses and redshifts; mass proxy, *mp*; mass proxy plus LSST-like photo-*z*, *mpz*), normalised to the *MATCH* reference of the same realism. The *FULL-FIX* distortion stays large and roughly constant, the *S-FIX* effect stays negligible, and the *NO-SSC* underestimation shrinks toward zero as the proxy scatter lowers the relative weight of the SSC term.

degeneracy of cluster observables and is therefore the best-constrained combination in the cluster posterior. It is the natural parameter along which the consistency between cluster counts and CMB constraints is assessed, and it is the S_8 error that directly sets the significance of the tension. Concretely, the tension significance between clusters (A) and the CMB (B) is

$$n_\sigma = \frac{|S_8^{(A)} - S_8^{(B)}|}{\sqrt{\sigma_A^2 + \sigma_B^2}}, \quad (4.4)$$

[48]. When the cluster uncertainty dominates ($\sigma_A \gg \sigma_B$), a fractional mis-estimate $\sigma_A \rightarrow f \sigma_A$ maps any true tension n_σ to a reported value $n_\sigma^{\text{rep}} = n_\sigma/f$: a factor-of- f error in σ_A produces an identical factor in the stated significance.

From table 3, the worst-case distortion of the marginal S_8 standard deviation occurs under *FULL-FIX* with $\Delta\sigma_8 = +0.10$, where the S_8 error is overestimated by +28%, and with $\Delta\sigma_8 = -0.10$, where it is underestimated by -31% (idealised, no-proxy case). The marginal σ_8 uncertainty is affected even more strongly in the same cases (+37% and -37%). However, as discussed above, σ_8 conflates the parameter-degeneracy direction with the direction of the observed tension, making it a less relevant summary statistic. The shot-noise-only (*NO-SSC*) limit underestimates the S_8 error by $\sim 30\%$. A similar result holds when we include the mass-proxy and photo-*z* scatter: the *FULL-FIX* distortion of the S_8 standard deviation reaches +34%/−28% for the mass-proxy catalog (*mp*) and +31%/−29% for the mass-proxy-plus-photo-*z* catalog (*mpz*), both essentially unchanged from the idealised case (table 3).

The sign follows the assumed amplitude: a covariance fixed at too low a fluctuation amplitude underestimates σ_A , inflating the apparent tension, while too high an amplitude softens it. Applying eq. (4.4) in the cluster-dominated limit, a genuine 2σ S_8 tension with $f = 1.28$ (+28% overestimate) would be reported as $2/1.28 \approx 1.6\sigma$, while $f = 0.69$ (−31% underestimate) gives $2/0.69 \approx 2.9\sigma$.

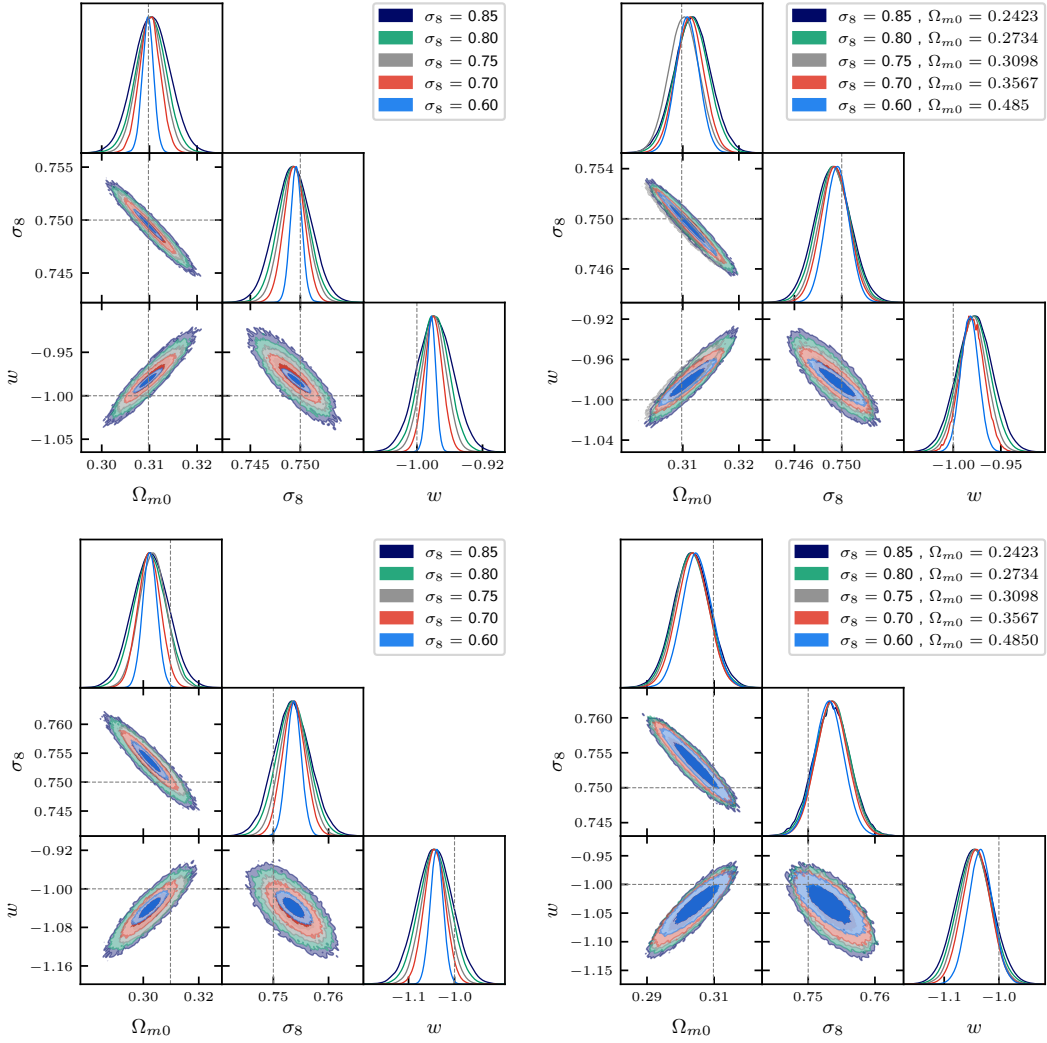


Figure 11: Corner plots for the cosmological parameters $\{\Omega_{m0}, \sigma_8, w\}$, with sky coverage $\Omega_{\text{sky}} = 18000 \text{ deg}^2$ and maximum redshift $z_{\text{max}} = 1.5$. Upper (lower) panels correspond to analyses assuming no-proxy (*mpz*). Contours denote the 68% and 95% confidence regions of the parameter posteriors. Left (right) panels show results obtained from MCMC when varying S_8 (S_8 fixed). Grey contours correspond to analyses in which the covariance matrix is fixed to the fiducial cosmology $\{\Omega_{m0} = 0.3098, \sigma_8 = 0.75, w = -1.0\}$, while the remaining cases assume covariance matrices fixed to shifted cosmological models, as indicated in the legend.

Thus, the same underlying discrepancy can appear substantially weaker or stronger solely because of the cosmology assumed when fixing the covariance.

Up to this point we have considered single-parameter sweeps and found that variations in σ_8 produce the largest covariance-induced distortions. However, changing σ_8 also changes $S_8 \equiv \sigma_8 \sqrt{\Omega_m/0.3}$, the parameter combination that is most tightly constrained by cluster counts and along which tensions with early-time probes are commonly quantified. To disentangle these effects, we extend the analysis in two

directions. First, we increase the range of the σ_8 scan from the $\Delta\sigma_8 = \pm 0.10$ variations considered above to $\sigma_8 = 0.60\text{--}0.85$ (table 2, upper), establishing a baseline for the large-mismatch regime. Second, we repeat the scan while adjusting Ω_{m0} so as to keep $S_8 = 0.762$, equal to its fiducial value (table 2, lower). This comparison isolates the extent to which the covariance response is associated with changes in S_8 itself, rather than with variations in σ_8 at fixed Ω_{m0} . Moreover, we focus on an LSST-like catalog with $z_{\text{max}} = 1.5$ and an area of $18\,000\text{ deg}^2$, and consider two observational scenarios: one using true masses and redshifts, and another incorporating mass-proxy and photometric-redshift uncertainties.

To probe the large-mismatch regime, we replace the marginal standard deviation with the full confidence-region volume $\Delta V/V_{\text{match}}$ and scan fixed covariance amplitudes over the wide range $\sigma_8 = 0.60\text{--}0.85$, bracketing the true fiducial $(\Omega_{m0}, \sigma_8, w) = (0.3098, 0.75, -1)$, for both idealised and mass-proxy-plus-photo- z catalogs (figure 11). We perform this scan in two complementary ways (18 MCMC analyses): (i) varying σ_8 alone, so that S_8 also changes (table 2, upper), and (ii) moving along the (Ω_{m0}, σ_8) degeneracy at fixed $S_8 = 0.762$ (table 2, lower), which isolates the S_8 -aligned response identified in section 4.1.

Table 2: Relative difference in the confidence-region volume, $\Delta V/V_{\text{match}}$, for different fixed-covariance cosmologies relative to the fiducial $(\Omega_{m0}, \sigma_8, w) = (0.3098, 0.75, -1)$. The triplet $(\Delta\Omega_m, \Delta\sigma_8, \Delta w)$ denotes the fractional change in the marginal standard deviation of $(\Omega_{m0}, \sigma_8, w)$ relative to the matched-covariance run (see eq. (4.2)). The upper group keeps Ω_{m0} at its fiducial value while varying σ_8 (and hence S_8); the lower group holds $S_8 = 0.762$ fixed and moves along the (Ω_{m0}, σ_8) degeneracy.

(Ω_{m0}, σ_8)	$(\Delta\Omega_m, \Delta\sigma_8, \Delta w)$	$\Delta V/V_{\text{match}}$ (true)	$\Delta V/V_{\text{match}}$ (<i>mpz</i>)
$\Omega_{m0} = 0.3098$ (fiducial); σ_8 varied (S_8 changes)			
(0.3098, 0.60)	(−57%, −57%, −63%)	−95%	−87%
(0.3098, 0.70)	(−21%, −20%, −24%)	−56%	−44%
(0.3098, 0.80)	(+19%, +18%, +24%)	+89%	+77%
(0.3098, 0.85)	(+40%, +38%, +50%)	+225%	+181%
$S_8 = 0.762$ fixed; (Ω_{m0}, σ_8) varied along the degeneracy			
(0.4850, 0.60)	(−23%, −23%, −36%)	−76%	−47%
(0.3567, 0.70)	(−8%, −8%, −13%)	−35%	−19%
(0.2734, 0.80)	(+10%, +9%, +15%)	+48%	+26%
(0.2423, 0.85)	(+19%, +18%, +31%)	+112%	+60%

The credible volume now changes by -87% to $+181\%$ across the assumed amplitudes in the *mpz* case (table 2, upper), and for the most discrepant covariance ($\sigma_8 = 0.60$) the posterior is compressed so strongly that the true cosmology falls outside the 95% region for both no-proxy and *mpz* cases (see left panels of figure 11): an apparent tension produced entirely by the covariance choice, with no shift in the underlying model. The comparison with the fixed- S_8 construction confirms that the effect is governed by the mismatch in S_8 : holding S_8 fixed while moving along the (Ω_{m0}, σ_8) degeneracy roughly halves the volume change (for example $-87\% \rightarrow -47\%$ at the lowest amplitude in the *mpz* case; table 2, lower), consistent with the S_8 -aligned response identified in section 4.1, see also the right panels of figure 11. Including mass-proxy and photometric-redshift uncertainties further reduces the discrepancy, in line with section 4.5.

These results show that neglecting the cosmology dependence of the covariance can materially misstate the significance of the S_8 tension between early- and late-time probes, even though it leaves the recovered cosmology unchanged. A consistent cosmology-dependent treatment of the covariance is therefore essential not only for parameter inference but also for robust assessments of cosmological tensions in the precision-cosmology era.

Table 3: Marginal standard deviations of S_8 and σ_8 at the worst-case survey layout ($\Omega_{\text{sky}} = 18000 \text{ deg}^2$, $z_{\text{max}} = 0.8$), for each covariance specification (S-FIX and FULL-FIX), proxy class (no-proxy, mp , mpz), and the largest parameter displacements used in this analysis ($|\Delta\Omega_{m0}| = 0.06$, $|\Delta\sigma_8| = 0.10$, $|\Delta w| = 0.40$). The ratio columns give the fractional change relative to the correctly-specified (MATCH, S-FIX) run within each proxy class; that reference row is marked ‘ref’. Positive ratios indicate an overestimate of the uncertainty, negative ratios an underestimate. Note that the worst-case distortions of the S_8 error are due shifts in σ_8 .

covariance	proxy	configuration	shift	std(S_8)	ratio	std(σ_8)	ratio
S-FIX	-	MATCH	-	0.0058	ref	0.0024	ref
FULL-FIX	-	MATCH	-	0.0057	-0.9%	0.0024	-0.3%
S-FIX	-	NO-SSC	-	0.0041	-29.5%	0.0019	-22.5%
FULL-FIX	-	NO-SSC	-	0.0041	-28.7%	0.0019	-22.2%
S-FIX	-	$\Delta\Omega_{m0}$	0.06	0.0052	-9.3%	0.0022	-8.6%
FULL-FIX	-	$\Delta\Omega_{m0}$	0.06	0.0064	11.4%	0.0027	10.2%
S-FIX	-	$\Delta\Omega_{m0}$	-0.06	0.0066	13.9%	0.0027	12.0%
FULL-FIX	-	$\Delta\Omega_{m0}$	-0.06	0.0049	-14.9%	0.0022	-11.5%
S-FIX	-	$\Delta\sigma_8$	0.10	0.0061	5.5%	0.0026	5.7%
FULL-FIX	-	$\Delta\sigma_8$	0.10	0.0074	27.6%	0.0033	36.5%
S-FIX	-	$\Delta\sigma_8$	-0.10	0.0053	-7.7%	0.0023	-5.4%
FULL-FIX	-	$\Delta\sigma_8$	-0.10	0.0040	-31.1%	0.0015	-36.5%
S-FIX	-	Δw	0.40	0.0060	4.8%	0.0026	7.4%
FULL-FIX	-	Δw	0.40	0.0052	-10.6%	0.0021	-12.8%
S-FIX	-	Δw	-0.40	0.0054	-6.0%	0.0023	-6.2%
FULL-FIX	-	Δw	-0.40	0.0063	8.7%	0.0026	8.1%
S-FIX	mp	MATCH	-	0.0070	ref	0.0034	ref
FULL-FIX	mp	MATCH	-	0.0072	3.1%	0.0033	-0.5%
S-FIX	mp	NO-SSC	-	0.0064	-8.2%	0.0032	-3.2%
FULL-FIX	mp	NO-SSC	-	0.0065	-6.9%	0.0033	-2.0%
S-FIX	mp	$\Delta\Omega_{m0}$	0.06	0.0070	-0.5%	0.0033	-0.9%
FULL-FIX	mp	$\Delta\Omega_{m0}$	0.06	0.0084	20.3%	0.0039	15.5%
S-FIX	mp	$\Delta\Omega_{m0}$	-0.06	0.0076	8.2%	0.0034	0.1%
FULL-FIX	mp	$\Delta\Omega_{m0}$	-0.06	0.0059	-15.3%	0.0028	-17.5%
S-FIX	mp	$\Delta\sigma_8$	0.10	0.0072	2.9%	0.0034	0.1%
FULL-FIX	mp	$\Delta\sigma_8$	0.10	0.0094	33.8%	0.0045	34.2%
S-FIX	mp	$\Delta\sigma_8$	-0.10	0.0070	-0.6%	0.0034	0.1%
FULL-FIX	mp	$\Delta\sigma_8$	-0.10	0.0051	-27.7%	0.0023	-32.4%
S-FIX	mp	Δw	0.40	0.0072	2.3%	0.0034	0.2%
FULL-FIX	mp	Δw	0.40	0.0064	-8.5%	0.0029	-13.5%
S-FIX	mp	Δw	-0.40	0.0071	0.9%	0.0033	-1.3%
FULL-FIX	mp	Δw	-0.40	0.0079	13.4%	0.0036	8.7%
S-FIX	mpz	MATCH	-	0.0075	ref	0.0034	ref
FULL-FIX	mpz	MATCH	-	0.0076	1.6%	0.0033	-1.0%
S-FIX	mpz	NO-SSC	-	0.0068	-10.3%	0.0033	-3.1%
FULL-FIX	mpz	NO-SSC	-	0.0069	-7.7%	0.0033	-3.2%
S-FIX	mpz	$\Delta\Omega_{m0}$	0.06	0.0072	-3.8%	0.0033	-1.7%
FULL-FIX	mpz	$\Delta\Omega_{m0}$	0.06	0.0089	18.6%	0.0038	14.2%
S-FIX	mpz	$\Delta\Omega_{m0}$	-0.06	0.0080	5.9%	0.0034	1.9%
FULL-FIX	mpz	$\Delta\Omega_{m0}$	-0.06	0.0063	-16.9%	0.0028	-16.4%
S-FIX	mpz	$\Delta\sigma_8$	0.10	0.0077	2.5%	0.0034	0.6%
FULL-FIX	mpz	$\Delta\sigma_8$	0.10	0.0099	31.3%	0.0045	34.7%
S-FIX	mpz	$\Delta\sigma_8$	-0.10	0.0075	-0.9%	0.0033	-1.1%
FULL-FIX	mpz	$\Delta\sigma_8$	-0.10	0.0054	-28.8%	0.0023	-32.1%
S-FIX	mpz	Δw	0.40	0.0077	1.9%	0.0034	0.1%
FULL-FIX	mpz	Δw	0.40	0.0068	-9.4%	0.0029	-13.1%
S-FIX	mpz	Δw	-0.40	0.0075	-0.9%	0.0034	-0.5%
FULL-FIX	mpz	Δw	-0.40	0.0083	10.1%	0.0037	8.7%

4.7 Covariance matrix fixed to the best-fit

Given that the dominant impact of fixing the covariance matrix concerns the inferred parameter uncertainties rather than the location of the maximum likelihood itself, we now explore an iterative strategy in which the covariance matrix is recalculated at the recovered best-fit cosmology. The motivation for this approach is that the previous analyses indicate that covariance misspecification primarily distorts the uncertainty normalization and the geometry of the confidence regions, while leaving the cosmological parameter estimators nearly unbiased.

Specifically, we first estimate the best-fit parameters using a fixed covariance matrix, and subsequently recompute the covariance matrix at the recovered best-fit values in order to derive the final cosmological constraints.

For this test, we consider the mirror-analysis configuration discussed in the previous sections. We generate mock realizations at the cosmologies $(\Omega_{m0}, \sigma_8, w) = (0.3098, 0.75, -1.0)$ and $(0.6486, 0.95, -2.0)$, while fixing the covariance matrix to that of the fiducial Λ CDM model of eq. (4.1). The first cosmology corresponds to the fiducial model adopted in section 4.6 and differs from the reference cosmology only through the value of σ_8 , thereby providing a direct connection with the results presented there. The second cosmology represents a more extreme departure from the fiducial model and probes a different region of parameter space. For each cosmology, we generate a single realization assuming a LSST-like survey configuration with area $\Omega_{\text{sky}} = 18000, \text{deg}^2$ and maximum redshift $z_{\text{max}} = 1.5$. The analyses are performed for both idealized (*no-proxy*) and more realistic (*mpz*) catalogs with $\sigma_0^{\text{ph}} = 0.03$.

The results, summarized in table 4, demonstrate that the relative difference in confidence-region volume, $\Delta V/V_{\text{match}}$, is dramatically reduced once the covariance matrix is recomputed at the recovered best-fit cosmology. For the iterated covariance, table 4 reports the volume differences of both the 1σ and 2σ confidence regions, see also figure 12. Unlike most of the models considered in this work, these cases exhibit a small but noticeable dependence on the confidence level, indicating that the covariance mismatch affects the tails of the posterior somewhat differently from the central region. Nevertheless, a single covariance update reduces the volume discrepancy from roughly 90% to only a few percent. Since the confidence-region volume depends on the full parameter covariance matrix, including all variances and correlations, the corresponding changes in the marginalized uncertainties of individual parameters are expected to be even smaller.

This confirms that a single covariance update at the recovered best-fit cosmology is sufficient to restore the correct uncertainty normalization. The reason is that the cosmology dependence of the covariance is smooth on the scale of the parameter uncertainties: from the slope of the FULL-FIX response in section 4.1 (a $\pm 37\%$ change in the σ_8 width over $\Delta\sigma_8 = \pm 0.10$), a 1σ error in the recovered σ_8 shifts the inferred widths by less than 1%, and only a few percent even at 3σ . A single update therefore lands the covariance close enough to the truth that the residual distortion is negligible. In practice, fixing the covariance matrix at a statistically supported cosmology provides an effective approximation, reducing computational cost while maintaining accurate parameter uncertainties and improving MCMC convergence.

Table 4: Relative difference in confidence-region volume, $\Delta V/V_{\text{match}}$, for analyses performed with a shifted covariance and after one covariance iteration. The iterated covariance is obtained by recomputing the covariance at the recovered best-fit parameters and rerunning the analysis. Before the iteration, the covariance is fixed at the fiducial model given in eq. (4.1).

Model	Simulation cosmology	Recovered best fit	Shifted	Iterated (1σ)	Iterated (2σ)
no-proxy	(0.3098, 0.75, -1.0)	(0.3118, 0.746, -0.982)	-95%	-2%	-2%
	(0.6486, 0.95, -2.0)	(0.6556, 0.946, -1.936)	-92%	1%	2%
<i>mpz</i>	(0.3098, 0.75, -1.0)	(0.3048, 0.753, -1.039)	-87%	2%	3%
	(0.6486, 0.95, -2.0)	(0.6416, 0.953, -2.039)	-94%	3%	1%

Two caveats qualify this conclusion. First, the procedure recomputes the covariance at the best fit, so it relies on that best fit being close to the truth, which in turn relies on the data constraining the cosmology tightly. The forecasts here neglect completeness, purity and other observational systematics, so the constraints we report are optimistic; with a fuller systematic budget the cluster posterior broadens, the best fit can fluctuate further from the truth, and the recomputed covariance becomes a correspondingly poorer estimate. The smoothness of $C(\theta)$ keeps even a several- σ excursion of the best-fit at the few-percent level, but the sub-percent margin quoted above is specific to our error budget and should be re-validated against the actual, systematics-inflated constraint of a given survey. Because $C(\hat{\theta})$ is a smooth model function of the best fit rather than a covariance estimated from the data, it requires no Hartlap-type correction, and the residual data dependence, entering only through $\hat{\theta}$, is second order and negligible.

Second, in a multi-probe analysis the covariance must be recomputed at the *cluster-counts-only* best fit, not at a joint one: a combined fit would place C at a cosmology that the clusters alone do not prefer. This holds even in the absence of any tension. Where early- and late-time probes are genuinely discrepant the single best fit is ambiguous, and a fully cosmology-dependent covariance, capable of consistently accommodating the parameter differences, remains necessary (section 4.6).

5 Conclusions

In this work we have investigated how assumptions about the covariance matrix of galaxy cluster number counts propagate into the inference of cosmological parameters, in particular Ω_{m0} , σ_8 , and w . Cluster abundances provide strong constraints on cosmology, but their likelihood depends not only on the mean counts but also on their covariance, which includes contributions from Poisson shot noise and super-sample covariance (SSC) induced by long-wavelength matter density fluctuations. Since both the signal and its covariance depend on cosmology, parameter inference ideally requires a fully cosmology-dependent treatment of the likelihood. In practice, however, the covariance, and especially its expensive SSC term, is often evaluated at a single fixed fiducial model for reasons of computational cost.

To quantify the consequences, we re-analysed a single realistic fiducial mock per survey layout under a controlled set of covariance constructions: fixing only the SSC kernel S while recomputing the abundance and bias prefactors (S-FIX), fixing the entire covariance (FULL-FIX), and dropping the SSC term altogether (NO-SSC), each evaluated either at the true cosmology (MATCH) or at a displaced one. Because all variants act on the *same* data vector, any change is attributable solely to the covariance choice. We probed the effect in two equivalent ways, a *forward* configuration that displaces the covariance on a fiducial mock and a realistic *mirror* configuration that displaces the data while holding the covariance at the fiducial value, and we characterised it through individual MCMC posterior widths and a Monte Carlo ensemble of best fits.

The cosmological parameter estimators remain unbiased under covariance misspecification. Across the entire scan over displacements, layouts and covariance constructions, the recovered means depart from the reference analysis by at most $\sim 1\%$ (largest for w , and below 0.5% for Ω_{m0} and σ_8), well within the parameter uncertainties ($\ll 1\sigma$); a Monte Carlo ensemble of $N = 1000$ mocks confirms a residual bias below 0.1σ in both the *forward* and *mirror* configurations. The dominant impact of covariance misspecification is therefore not a shift in the best-fit parameters, but a modification of the inferred parameter uncertainties and of the geometry of the confidence regions.

Fixing the covariance is not, in itself, the source of error: under FULL-FIX at the *true* cosmology the posterior widths are indistinguishable from MATCH ($R_\theta = 1.00$). The error arises only when the covariance is fixed at the *wrong* cosmology, and its size depends strongly on which ingredients are frozen. Freezing only the S matrix (S-FIX) while keeping the counts and bias consistent has a minor impact, with width changes $\lesssim 6\%$ on σ_8 and $\lesssim 12\%$ on Ω_{m0} even for the largest displacements. Fixing the full covariance (FULL-FIX), by contrast, distorts the widths substantially and monotonically: for σ_8 we find a $\pm 37\%$ mis-estimation at $\Delta\sigma_8 = \pm 0.10$, a covariance built at a lower (higher) power spectrum amplitude yielding

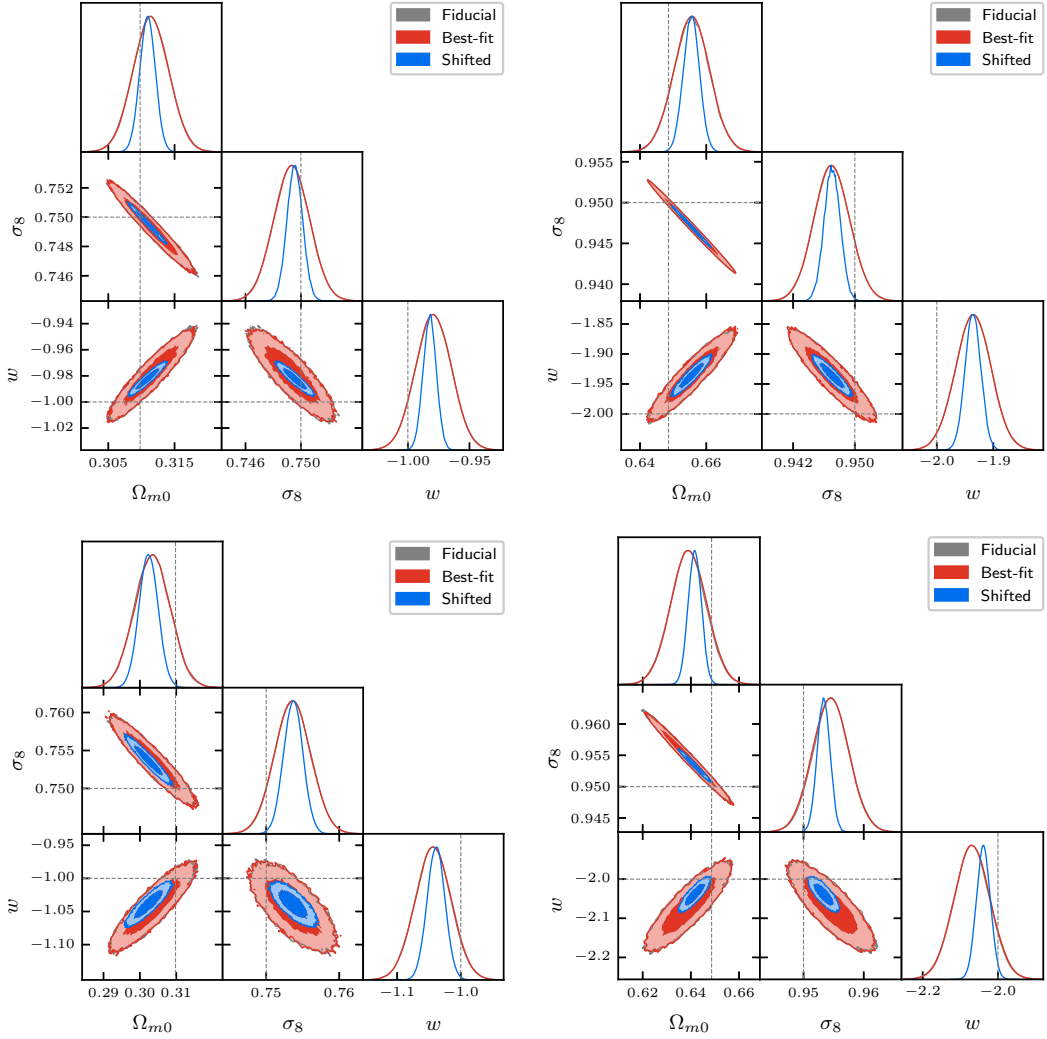


Figure 12: Corner plots for the cosmological parameters $\{\Omega_{m0}, \sigma_8, w\}$ comparing analyses performed with a matched covariance (gray), a shifted covariance fixed at the fiducial model of eq. (4.1) (blue), and an iterated covariance obtained by recomputing the covariance at the recovered best-fit cosmology (red). The top(bottom) panels show the no-proxy(*mpz*) analyses. The left and right panels show the mirror-analysis realizations generated at $(\Omega_{m0}, \sigma_8, w) = (0.3098, 0.75, -1.0)$ and $(0.6486, 0.95, -2.0)$, respectively, following table 4. Contours denote the 68% and 95% credible regions.

artificially tight (broad) posteriors. Since the S matrix is the computationally expensive ingredient, the robustness of S-FIX is a useful practical result.

The contrast between S-FIX and FULL-FIX identifies where the cosmology dependence of the covariance actually resides. Their only difference is whether the abundance and bias prefactors $b\bar{\mu}$ are recomputed or frozen, so the fact that S-FIX is nearly harmless while FULL-FIX is not shows that the dominant cosmology dependence of the cluster-count covariance lies in these prefactors rather than in the S matrix itself. This is physically expected: the cluster abundance is exponentially sensitive to the

amplitude of matter fluctuations, so freezing $b\bar{\mu}$ at a wrong amplitude strongly mis-scales the SSC term, whereas S varies comparatively slowly with cosmology.

Although variations in Ω_{m0} and σ_8 do not produce a simple monotonic behaviour when considered individually, the dominant trends are organised by the derived parameter S_8 . Since cluster counts primarily constrain a degenerate combination of Ω_{m0} and σ_8 , the effect of covariance misspecification projects mainly along this direction and acts as an effective rescaling of the uncertainties along the S_8 degeneracy axis. The impact of covariance assumptions depends more strongly on survey characteristics than on the dark energy equation of state: variations in w have a subdominant effect, whereas the survey area is decisive, wide-field configurations coupling most strongly to the large-scale modes that enter the SSC term. Consistently, the NO-SSC construction underestimates the uncertainties by $\sim 25\%$ on σ_8 at $\Omega_{\text{sky}} = 18000 \text{ deg}^2$, falling to $\sim 5\%$ at 3000 deg^2 , with only a weak dependence on depth.

The *forward* and *mirror* configurations yield the same result once both are expressed in terms of the mismatch between the data and covariance cosmologies. The impact of covariance misspecification depends only on this mismatch and not on which of the two is displaced, so the controlled forward scan is representative of a real analysis, in which the covariance is fixed at an assumed cosmology while the data correspond to the unknown true one. As a complementary measure to the marginal widths we also report the joint credible volume, which additionally captures changes in the correlation structure of the parameters: under FULL-FIX it changes by up to $+132\%$ and -67% at $\Delta\sigma_8 = \pm 0.10$, and the same volume is recovered either as the highest-posterior -density volume of the MCMC chains or as $\sqrt{\det \text{Cov}}$ of the Monte Carlo best-fit ensemble.

These results are robust to observational realism. Repeating the worst-case analysis with a mass proxy and with LSST-like photometric redshifts broadens the constraints by up to $\sim 50\%$ but leaves the covariance-misspecification effects essentially unchanged: the FULL-FIX distortion stays at the $\pm 35\%$ level on σ_8 and the estimators remain unbiased, while the shot-noise-only (NO-SSC) underestimation is the one effect that mildly relaxes, as the proxy scatter lowers the relative weight of the SSC term.

This width effect propagates directly into cosmological tension. Because covariance misspecification rescales the parameter uncertainties without moving the estimators, it rescales the statistical *significance* of the σ_8/S_8 tension between cluster counts and early-time probes without creating or removing it. In the regime where the cluster measurement dominates the combined uncertainty, the $\pm 37\%$ mis-estimation of the σ_8 width turns a nominal 2σ tension into anywhere from $\sim 1.6\sigma$ to $\sim 2.9\sigma$ depending only on the cosmology assumed for the covariance, and in extreme cases the distortion is large enough to place the true cosmology outside the 95% region.

A simple mitigation is available for single-probe analyses: because the estimators are unbiased and the covariance varies smoothly on the scale of the parameter uncertainties (a 1σ error in σ_8 changes the widths by less than 1%), recomputing the covariance once at the recovered best fit restores the correct uncertainties even when starting from a badly misspecified covariance. Two qualifications apply. The constraints forecast here are optimistic, as they omit cluster completeness and purity and other observational systematics; a wider, more realistic posterior lets the best fit fluctuate further from the truth, so the sub-percent margin should be re-validated against a survey's actual constraint. And in a multi-probe setting the covariance must be recomputed at the cluster-counts-only best fit, not at a joint one.

For multi-probe analyses combining early- and late-time observables, a fully cosmology-dependent treatment of the covariance matrix remains necessary to ensure internal consistency and to avoid propagating mismatches between probes. Overall, our results demonstrate that the dominant cosmology dependence of the cluster-count covariance arises from the abundance and bias prefactors and their sensitivity to the amplitude of matter fluctuations, that this dependence projects naturally onto the S_8 degeneracy direction, and that a consistent cosmology-dependent treatment of the covariance matrix is essential for robust cluster cosmology analyses and for reliable assessments of concordance or tension between early- and late-time probes in the precision era of large-scale structure surveys.

A Estimation of Posterior Credible Volumes from MCMC Chains

In this work, parameter constraints are quantified through the volume of the N -dimensional highest-posterior-density (HPD) region enclosing a credible fraction α of the posterior distribution. This appendix summarizes the numerical procedure used to estimate this volume from MCMC samples.

Let $P(\vec{\theta}|D)$ denote the posterior distribution for the parameter vector $\vec{\theta}$. In particular, $\vec{\theta} = \{\Omega_{m0}, \sigma_8, w\}$. The HPD region Ω_α is defined such that

$$\alpha = \frac{\int_{\Omega_\alpha} P(\vec{\theta}|D) d\Omega_\theta}{\int_{\Omega_{\text{total}}} P(\vec{\theta}|D) d\Omega_\theta}, \quad (\text{A.1})$$

where α typically takes the values 0.6827 or 0.9545. The associated credible volume is

$$V = \int_{\Omega_\alpha} d\Omega_\theta. \quad (\text{A.2})$$

In practice, the HPD region is approximated directly from the MCMC chain of size N_{chain} . The samples are sorted in decreasing order of posterior probability (equivalently, increasing order of $-2 \ln P$). The first

$$N = \text{int}(\alpha N_{\text{chain}})$$

samples define the discrete approximation to Ω_α .

From this subset, we compute

$$s = \sum_{i=1}^N \exp \left[\frac{-2 \ln P_i - (-2 \ln P_{\text{bf}})}{2} \right], \quad (\text{A.3})$$

where P_{bf} denotes the posterior evaluated at the maximum (best-fit) point.

The logarithmic volume is then estimated as

$$\ln V = \ln(P_{\text{norm}}) - \ln P_{\text{bf}} + \ln \left(\frac{s}{N_{\text{chain}}} \right), \quad (\text{A.4})$$

where P_{norm} is the posterior normalization constant. The credible volume V is obtained by exponentiation.

This estimator provides a numerical approximation to the HPD credible volume directly from the MCMC samples, avoiding assumptions about Gaussianity or parameter degeneracy structure. It is implemented in NumCosmo [54] as the `get_post_lnv01` method of the Monte Carlo catalogue class, which we use to compute all credible volumes reported in this work.

Gaussian limit and the Monte Carlo estimate

The estimator of eq. (A.4) is non-parametric, but it is instructive to connect it to the Gaussian approximation and to the Monte Carlo ensemble of section 4.4. If the posterior is approximately Gaussian with covariance C in d dimensions, the HPD region at level α is the ellipsoid $\{\vec{\theta} : (\vec{\theta} - \vec{\mu})^\top C^{-1} (\vec{\theta} - \vec{\mu}) \leq \chi_d^2(\alpha)\}$, with $\chi_d^2(\alpha)$ the corresponding quantile of the chi-squared distribution with d degrees of freedom. Its volume is

$$V_\alpha = \frac{\pi^{d/2}}{\Gamma(d/2 + 1)} [\chi_d^2(\alpha)]^{d/2} \sqrt{\det C}, \quad (\text{A.5})$$

so that, at fixed credible level and dimension, $V_\alpha \propto \sqrt{\det C}$.

Equation (A.5) provides a second, independent route to the same volume. From the Monte Carlo ensemble of section 4.4 we form the sample covariance \hat{C} of the N best-fit estimates and evaluate $\sqrt{\det \hat{C}}$. Because the chain-based estimator of eq. (A.4) makes no Gaussianity assumption, whereas

$\sqrt{\det \hat{C}}$ does through eq. (A.5), their agreement (section 4.4) simultaneously confirms that the posterior is close to Gaussian over the relevant region and that the width of the MCMC posterior faithfully tracks the frequentist scatter of the estimator across realizations. We therefore use the two readings of the credible volume, from the posterior chain and from the ensemble of estimators, interchangeably in the main text.

Acknowledgments

HCNL acknowledges the support of the Coordenação de Aperfeiçoamento de Pessoal de Nível Superior (CAPES) under grant 88887704526/2022-00. All authors acknowledge the support of Fundação Araucária (NAPI de Fenômenos Extremos do Universo, Grant No. 347/2024 PDI).

References

- [1] S.W. Allen, A.E. Evrard and A.B. Mantz, *Cosmological Parameters from Observations of Galaxy Clusters*, *Annual Review of Astronomy and Astrophysics* **49** (2011) 409 [1103.4829].
- [2] A.V. Kravtsov and S. Borgani, *Formation of Galaxy Clusters*, *Annual Review of Astronomy and Astrophysics* **50** (2012) 353 [1205.5556].
- [3] Planck Collaboration, P.A.R. Ade, N. Aghanim, M. Arnaud, M. Ashdown, J. Aumont et al., *Planck 2015 results. XXIV. Cosmology from Sunyaev-Zeldovich cluster counts*, *Astronomy & Astrophysics* **594** (2016) A24 [1502.01597].
- [4] E. Lee, R. Battye and B. Bolliet, *Cosmological inference from combining Planck and ACT cluster counts*, *Monthly Notices of the Royal Astronomical Society* **538** (2025) 2768 [2403.19542].
- [5] A. Mantz, S.W. Allen, D. Rapetti and H. Ebeling, *The observed growth of massive galaxy clusters - I. Statistical methods and cosmological constraints*, *Monthly Notices of the Royal Astronomical Society* **406** (2010) 1759 [0909.3098].
- [6] S. Bocquet, J.P. Dietrich, T. Schrabback, L.E. Bleem, M. Klein, S.W. Allen et al., *Cluster Cosmology Constraints from the 2500 deg² SPT-SZ Survey: Inclusion of Weak Gravitational Lensing Data from Magellan and the Hubble Space Telescope*, *The Astrophysical Journal* **878** (2019) 55 [1812.01679].
- [7] I.-N. Chiu, M. Klein, J. Mohr and S. Bocquet, *Cosmological constraints from galaxy clusters and groups in the eROSITA final equatorial depth survey*, *Monthly Notices of the Royal Astronomical Society* **522** (2023) 1601 [2207.12429].
- [8] V. Ghirardini, E. Bulbul, E. Artis, N. Clerc, C. Garrel, S. Grandis et al., *The SRG/eROSITA all-sky survey: Cosmology constraints from cluster abundances in the western Galactic hemisphere*, *Astronomy & Astrophysics* **689** (2024) A298 [2402.08458].
- [9] S. Bocquet, S. Grandis, L.E. Bleem, M. Klein, J.J. Mohr, T. Schrabback et al., *SPT clusters with DES and HST weak lensing. II. Cosmological constraints from the abundance of massive halos*, *Physical Review D* **110** (2024) 083510 [2401.02075].
- [10] E. Rozo, R.H. Wechsler, E.S. Rykoff, J.T. Annis, M.R. Becker, A.E. Evrard et al., *Cosmological Constraints from the Sloan Digital Sky Survey maxBCG Cluster Catalog*, *The Astrophysical Journal* **708** (2010) 645 [0902.3702].
- [11] M. Costanzi, E. Rozo, M. Simet, Y. Zhang, A.E. Evrard, A. Mantz et al., *Methods for cluster cosmology and application to the SDSS in preparation for DES Year 1 release*, *Monthly Notices of the Royal Astronomical Society* **488** (2019) 4779 [1810.09456].
- [12] T.M.C. Abbott, M. Aguena, A. Alarcon, S. Allam, S. Allen, J. Annis et al., *Dark Energy Survey Year 1 Results: Cosmological constraints from cluster abundances and weak lensing*, *Physical Review D* **102** (2020) 023509 [2002.11124].

- [13] T.M.C. Abbott, M. Aguena, A. Alarcon, A. Amon, D. Anbajagane, F. Andrade-Oliveira et al., *Dark energy survey year 3 results: Cosmological constraints from cluster abundances, weak lensing, and galaxy clustering*, *Physical Review D* **112** (2025) 083535 [2503.13632].
- [14] M. Maturi, A. Finoguenov, P.A.A. Lopes, R.M. González Delgado, R.A. Dupke, E.S. Cypriano et al., *The miniJPAS survey. Cluster and galaxy group detections with AMICO*, *Astronomy & Astrophysics* **678** (2023) A145 [2307.06412].
- [15] L. Doubrawa, E.S. Cypriano, A. Finoguenov, P.A.A. Lopes, A.H. Gonzalez, M. Maturi et al., *The miniJPAS survey. Optical detection of galaxy clusters with PZWav*, *Astronomy & Astrophysics* **685** (2024) A98 [2312.12197].
- [16] LSST Dark Energy Science Collaboration, *Large Synoptic Survey Telescope: Dark Energy Science Collaboration*, *arXiv e-prints* (2012) arXiv:1211.0310 [1211.0310].
- [17] R. Laureijs, J. Amiaux, S. Arduini, J.L. Auguères, J. Brinchmann, R. Cole et al., *Euclid Definition Study Report*, *arXiv e-prints* (2011) arXiv:1110.3193 [1110.3193].
- [18] E. Artis, E. Bulbul, S. Grandis, V. Ghirardini, N. Clerc, R. Seppi et al., *The srg/erosita all-sky survey-constraints on the structure growth from cluster number counts*, *Astronomy & Astrophysics* **696** (2025) A5 [2410.09499].
- [19] W. Hu and A.V. Kravtsov, *Sample variance considerations for cluster surveys*, *The Astrophysical Journal* **584** (2003) 702 [astro-ph/0203169].
- [20] P. Valageas, N. Clerc, F. Pacaud and M. Pierre, *Covariance matrices for halo number counts and correlation functions*, *Astronomy & Astrophysics* **536** (2011) A95 [1104.4015].
- [21] M. Takada and W. Hu, *Power spectrum super-sample covariance*, *Physical Review D* **87** (2013) [1302.6994].
- [22] M. Takada and D.N. Spergel, *Joint analysis of cluster number counts and weak lensing power spectrum to correct for the super-sample covariance*, *Monthly Notices of the Royal Astronomical Society* **441** (2014) 2456 [1307.4399].
- [23] F. Lacasa and R. Rosenfeld, *Combining cluster number counts and galaxy clustering*, *Journal of Cosmology and Astroparticle Physics* **2016** (2016) 005 [1603.00918].
- [24] F. Lacasa and J. Grain, *Fast and easy super-sample covariance of large scale structure observables*, *Astronomy & Astrophysics* **624** (2019) A61 [1809.05437].
- [25] S. Gouyou Beauchamps, F. Lacasa, I. Tutusaus, M. Aubert, P. Baratta, A. Gorce et al., *Impact of survey geometry and super-sample covariance on future photometric galaxy surveys*, *Astronomy & Astrophysics* **659** (2022) A128 [2109.02308].
- [26] F. Lacasa, M. Lima and M. Aguena, *Super-sample covariance approximations and partial sky coverage*, *Astronomy & Astrophysics* **611** (2018) A83 [1612.05958].
- [27] C. Payerne, C. Murray, C. Combet, C. Doux, A. Fumagalli and M. Penna-Lima, *Testing the accuracy of likelihoods for cluster abundance cosmology*, *Monthly Notices of the Royal Astronomical Society* **520** (2023) 6223 [2210.11093].
- [28] C. Payerne, C. Murray, C. Combet and M. Penna-Lima, *Towards including super-sample covariance in the unbinned likelihood for cluster abundance cosmology*, *Monthly Notices of the Royal Astronomical Society* (2024) stae1504 [2401.10024].
- [29] A. Fumagalli, A. Saro, S. Borgani, T. Castro, M. Costanzi, P. Monaco et al., *Euclid : Effects of sample covariance on the number counts of galaxy clusters*, *Astronomy & Astrophysics* **652** (2021) A21 [2102.08914].
- [30] F. Hofmann, J. Sanders, N. Clerc, K. Nandra, J. Ridl, K. Dennerl et al., *erosita cluster cosmology forecasts: Cluster temperature substructure bias*, *Astronomy & Astrophysics* **606** (2017) A118 [1708.05205].

- [31] F. Lacasa, M. Aubert, P. Baratta, J. Carron, A. Gorce, S.G. Beauchamps et al., *Efficient computation of the super-sample covariance for stage iv galaxy surveys*, *Astronomy & Astrophysics* **671** (2023) A115 [2209.14421].
- [32] E.E.O. Ishida, S.D.P. Vitenti, M. Penna-Lima, J. Cisewski, R.S. de Souza, A.M.M. Trindade et al., *COSMOABC: Likelihood-free inference via Population Monte Carlo Approximate Bayesian Computation*, *Astron. Comput.* **13** (2015) 1 [1504.06129].
- [33] Í. Zubeldia, B. Bolliet, A. Challinor and W. Handley, *Extracting cosmological information from the abundance of galaxy clusters with simulation-based inference*, *Physical Review D* **112** (2025) 083536 [2504.10230].
- [34] N. Cerardi, M. Pierre, F. Lanusse and X. Corap, *The Cosmological analysis of X-ray cluster surveys: VII. Bypassing scaling relations with Lagrangian Deep Learning and Simulation-based inference*, *Astronomy & Astrophysics* **701** (2025) A110 [2507.01820].
- [35] M. Ntampaka, A. Cipurjanovic, A.M. Delgado, J. Soltis, J.F. Wu, M. Yunus et al., *The Importance of Being Adaptable: An Exploration of the Power and Limitations of Domain Adaptation for Simulation-Based Inference with Galaxy Clusters*, *arXiv e-prints* (2025) arXiv:2510.09748 [2510.09748].
- [36] C. Payerne, C. Murray and H. Simon, *Simulation-based cosmological inference from optically-selected galaxy clusters with Capish*, *arXiv e-prints* (2026) arXiv:2602.01911 [2602.01911].
- [37] J. Prat, J. Zuntz, C. Chang, T. Tröster, E. Pedersen, C. García-García et al., *The catalog-to-cosmology framework for weak lensing and galaxy clustering for lsst*, *The Open Journal of Astrophysics* **6** (2023) [2212.09345].
- [38] A. Fumagalli, M. Costanzi, A. Saro, T. Castro and S. Borgani, *Cosmological constraints from the abundance, weak lensing, and clustering of galaxy clusters: Application to the SDSS*, *Astronomy & Astrophysics* **682** (2024) A148 [2310.09146].
- [39] C.M. Hirata, R. Mandelbaum, U. Seljak, J. Guzik, N. Padmanabhan, C. Blake et al., *Galaxy-galaxy weak lensing in the Sloan Digital Sky Survey: intrinsic alignments and shear calibration errors*, *Monthly Notices of the Royal Astronomical Society* **353** (2004) 529 [astro-ph/0403255].
- [40] J. Hartlap, P. Simon and P. Schneider, *Why your model parameter confidences might be too optimistic. unbiased estimation of the inverse covariance matrix*, *Astronomy & Astrophysics* **464** (2006) 399–404 [astro-ph/0608064].
- [41] T. Eifler, P. Schneider and J. Hartlap, *Dependence of cosmic shear covariances on cosmology-impact on parameter estimation*, *Astronomy & Astrophysics* **502** (2009) 721 [0810.4254].
- [42] R. Mandelbaum, A. Slosar, T. Baldauf, U. Seljak, C.M. Hirata, R. Nakajima et al., *Cosmological parameter constraints from galaxy-galaxy lensing and galaxy clustering with the SDSS DR7*, *Monthly Notices of the Royal Astronomical Society* **432** (2013) 1544 [1207.1120].
- [43] E. Krause and T. Eifler, *cosmolike – cosmological likelihood analyses for photometric galaxy surveys*, *Monthly Notices of the Royal Astronomical Society* **470** (2017) 2100 [1601.05779].
- [44] O. Friedrich and T. Eifler, *Precision matrix expansion - efficient use of numerical simulations in estimating errors on cosmological parameters*, *Monthly Notices of the Royal Astronomical Society* **473** (2018) 4150 [1703.07786].
- [45] S. Dodelson and M.D. Schneider, *The effect of covariance estimator error on cosmological parameter constraints*, *Physical Review D* **88** (2013) [1304.2593].
- [46] M. Penna-Lima, M. Makler and C.A. Wuensche, *Biases on cosmological parameter estimators from galaxy cluster number counts*, *Journal of Cosmology and Astroparticle Physics* **2014** (2014) 039 [1312.4430].
- [47] E. Abdalla, G.F. Abellán, A. Aboubrahim, A. Agnello, Ö. Akarsu, Y. Akrami et al., *Cosmology intertwined: A review of the particle physics, astrophysics, and cosmology associated with the cosmological tensions and anomalies*, *Journal of High Energy Astrophysics* **34** (2022) 49 [2203.06142].

- [48] I. Pantos and L. Perivolaropoulos, *Status of the S_8 Tension: A 2026 Review of Probe Discrepancies*, *arXiv e-prints* (2026) arXiv:2602.12238 [2602.12238].
- [49] PLANCK collaboration, *Planck 2018 results. VI. Cosmological parameters*, *Astron. Astrophys.* **641** (2020) A6 [1807.06209].
- [50] M. Asgari, C.-A. Lin, B. Joachimi, B. Giblin, C. Heymans, H. Hildebrandt et al., *Kids-1000 cosmology: Cosmic shear constraints and comparison between two point statistics*, *Astronomy & Astrophysics* **645** (2021) A104 [2007.15633].
- [51] R. Dalal, X. Li, A. Nicola, J. Zuntz, M.A. Strauss, S. Sugiyama et al., *Hyper supprime-cam year 3 results: Cosmology from cosmic shear power spectra*, *Physical Review D* **108** (2023) 123519.
- [52] T. Sunayama, H. Miyatake, S. Sugiyama, S. More, X. Li, R. Dalal et al., *Optical cluster cosmology with SDSS redMaPPer clusters and HSC-Y3 lensing measurements*, *Physical Review D* **110** (2024) 083511 [2309.13025].
- [53] H. Miyatake, *Cosmology with Galaxy Clusters*, *arXiv e-prints* (2025) arXiv:2505.07697 [2505.07697].
- [54] S. Dias Pinto Vitenti and M. Penna-Lima, “NumCosmo: Numerical Cosmology.” Astrophysics Source Code Library ascl:1408.013, Aug., 2014.
- [55] J. Tinker, A.V. Kravtsov, A. Klypin, K. Abazajian, M. Warren, G. Yepes et al., *Toward a halo mass function for precision cosmology: The limits of universality*, *The Astrophysical Journal* **688** (2008) 709 [0803.2706].
- [56] G. Despali, C. Giocoli, R.E. Angulo, G. Tormen, R.K. Sheth, G. Baso et al., *The universality of the virial halo mass function and models for non-universality of other halo definitions*, *Monthly Notices of the Royal Astronomical Society* **456** (2016) 2486 [1507.05627].
- [57] T. Kitayama and Y. Suto, *Semi-analytic predictions for statistical properties of x-ray clusters of galaxies in cold dark matter universes*, *The Astrophysical Journal* **469** (1996) 480 [astro-ph/9604141].
- [58] D.J. Eisenstein and W. Hu, *Baryonic features in the matter transfer function*, *The Astrophysical Journal* **496** (1998) 605 [astro-ph/9709112].
- [59] N. Kaiser, *On the spatial correlations of Abell clusters.*, vol. 284 (1984), 10.1086/184341.
- [60] H. Mo and S.D. White, *An analytic model for the spatial clustering of dark matter haloes*, *Monthly Notices of the Royal Astronomical Society* **282** (1996) 347 [astro-ph/9512127].
- [61] J.L. Tinker, B.E. Robertson, A.V. Kravtsov, A. Klypin, M.S. Warren, G. Yepes et al., *The large-scale bias of dark matter halos: Numerical calibration and model tests*, *The Astrophysical Journal* **724** (2010) 878 [1001.3162].
- [62] T. Ishiyama et al., *The Uchuu simulations: Data Release 1 and dark matter halo concentrations*, *Monthly Notices of the Royal Astronomical Society* **506** (2021) 4210 [2007.14720].
- [63] R. Murata, T. Nishimichi, M. Takada, H. Miyatake, M. Shirasaki, S. More et al., *Constraints on the mass–richness relation from the abundance and weak lensing of sdss clusters*, *The Astrophysical Journal* **854** (2018) 120 [1707.01907].
- [64] R. Mandelbaum, T. Eifler, R. Hložek, T. Collett, E. Gawiser, D. Scolnic et al., *The lsst dark energy science collaboration (desc) science requirements document*, *arXiv preprint arXiv:1809.01669* (2018) [1809.01669].
- [65] S. D P Vitenti and E.J. Barroso, *Apes: approximate posterior ensemble sampler*, *Monthly Notices of the Royal Astronomical Society* **525** (2023) 73 [2303.13667].